AN EXPERIMENTAL STUDY OF A STELLAR NEUTRON SOURCE: $^{13}C(\alpha, n)^{16}O$

Thesis by
Cary Nathan Davids

In Partial Fulfillment of the Requirements

For the Degree of
Doctor of Philosophy

California Institute of Technology
Pasadena, California
1967
(Submitted March 1, 1967)

ACKNOWLEDGMENTS

The author would like to thank the entire staff of the Kellogg Radiation Laboratory for the assistance and encouragement provided during the course of this work. Especially appreciated were the aid given by Professor W. A. Fowler, who initially suggested the project, and discussions with Professor C. A. Barnes, which led to many clarifications.

A Graduate Research Fellowship from Imperial Oil Limited of Canada is gratefully acknowledged, as is the support provided by the Office of Naval Research.

ABSTRACT

Described in this thesis are measurements made of the thick-target neutron yield from the reaction $^{13}C(\alpha, n)^{16}O$. The yield was determined for laboratory bombarding energies between 0.475 and 0.700 MeV, using a stilbene crystal neutron detector and pulse-shape discrimination to eliminate gamma rays. Stellar temperatures between 2.5 and 4.5 x 10^8 ^oK are involved in this energy region. From the neutron yield was extracted the astrophysical cross-section factor S(E), which was found to fit a linear function: $S(E) = [\ (5.48 \pm 1.77) + (12.05 \pm 3.91)E\ ] \times 10^5$ MeV-barns, center-of-mass system. The stellar rate of the $^{13}C(\alpha,n)^{16}O$ reaction is calculated, and discussed with reference to helium burning and neutron production in the core of a giant star.

Results are also presented of measurements carried out on the reaction $^{9}Be(\alpha, n)^{12}C$, taken with a thin Be target. The bombarding energy-range covered was from 0.340 to 0.680 MeV, with excitation curves for the ground- and first excited-state neutrons being reported. Some angular distributions were also measured. Resonances were found at bombarding energies of E_{LAB} = 0.520 MeV (E_{CM} = 0.360 MeV, $\Gamma \sim$ 55 keV CM, $\omega\gamma$ = 3.79 eV CM) and E_{LAB} = 0.600 MeV (E_{CM} = 0.415 MeV, $\Gamma <$ 4 keV CM, $\omega\gamma$ = 0.88 eV CM). The astrophysical rate of the $^{9}Be(\alpha, n)^{12}C$ reaction due to these resonances is calculated.

TABLE OF CONTENTS

I. INTRODUCTION

As part of the continuing program in the Kellogg-Sloan laboratories on the study of nuclear reactions in stars, the present investigation was undertaken on the reaction $^{13}C(\alpha, n)^{16}O$. Greenstein (1954) and Cameron (1954) first proposed this reaction as a source of stellar neutrons. At temperatures near 10^8 ^oK the neutrons are thermalized in the dense stellar medium, and are captured by heavy "seed" nuclei in great numbers. The seed nuclei, principally members of the iron group, are present in small amounts as part of the material from which the star originally condensed.

Jones and Wilkinson (1951) first experimentally observed the reaction, by bombarding a thick separated ^{13}C target with 1.05 MeV alpha particles. They reported further work (Jones 1953) in the energy range 1.0 to 2.1 MeV. Rusbridge (1956) extended their work up to 2.5 MeV, using better resolution. Walton et al (1957) measured the 0^o yield from 0.8 to 3.5 MeV, as well as yields at other angles at higher energies, and angular distributions above 1.0 MeV. No experimental work has been reported at lower energies, because of the very low yield of the reaction.

In order to determine the rate of the $^{13}C(\alpha, n)^{16}O$ reaction at stellar temperatures, one must know the cross-section below center-of-mass energies of about 0.3 MeV. Because of the high coulomb barrier between alpha particles and ^{13}C nuclei, the cross-section in this region is too low to measure at the present time. It is thus necessary to measure the cross-section in the laboratory down to as low a bombarding energy as is possible, and to rely on theory to predict the low-energy behaviour. For low-energy nuclear reactions one can write

$$\sigma(E) = \frac{S(E)\, e^{-2\pi\eta}}{E} \qquad (1)$$

where S(E) is called the cross-section factor. Here we are assuming that no resonances occur in the stellar thermal region. In this case S(E) is generally treated as a constant or as a constant plus a term linear in energy. If a resonance exists in the thermal region equation (1) is still valid, but a dispersion form must be ascribed to S(E). If there are more resonances, with the possibility of interference, S(E) becomes more complicated, and a theoretical extrapolation to lower energies becomes somewhat less reliable.

In the present experiment the yield of the reaction $^{13}C(\alpha, n)^{16}O$ has been determined for center-of-mass energies from 0.526 down to 0.373 MeV, and the cross-section factor has been fitted by the method of least squares to a function of the form S(E) = S(0) + (dS/dE)E.

In the course of developing a counter for use in this experiment, measurements were made on the reactions $^{9}Be(\alpha, n_0)^{12}C$ and $^{9}Be(\alpha, n_1)^{12}C^*(4.43)$. These reactions provided a readily available source of neutrons for testing purposes, and the second reaction also produces a 4.43 MeV gamma ray. In this way the neutron-gamma discriminator (to be described later) could be adjusted for optimum elimination of gamma radiation.

The $^{9}Be(\alpha, n)^{12}C$ reaction has long been known as a prolific source of neutrons (Chadwick 1932). Bennett, Roys, and Toppel (1954) first observed the two low-energy resonances around 0.6 MeV bombarding energy with good resolution. However, their work was presented in abstract, and the only published figures depicting their

results appeared in Amaldi's article in the Handbuch der Physik (1959). They used a BF_3 long counter to detect the neutrons, which did not allow a separation of the n_0 (ground-state) and n_1 (first excited-state) groups. James et al (1956) published the results of some of their earlier work, including analysis, but their data did not contain the two low-energy resonances. Instead, they observed a peak in the yield at a bombarding energy of about 0.650 MeV. They were able, on the basis of their angular distributions and the Bennett data, to tentatively assign a spin of $(1/2^+)$ to the 11.01 MeV level in ^{13}C. This is the level responsible for the resonance at 0.52 MeV bombarding energy in $^{9}Be(\alpha, n)^{12}C$. No information has been available on the state producing the resonance at 0.60 MeV, the 11.08 MeV state of ^{13}C.

Before beginning the experiments, a completely new beam handling system for the 700 kV accelerator in the Kellogg Radiation Laboratory was designed and built. The existing electrostatic analyser was removed and replaced by a 90^{o} magnetic analyser. Steering magnets, regulating and beam-defining slits, and cold traps were constructed and installed. An oil diffusion pump was obtained for use on the target side of the analyser, since the narrow beam tube of the analyser effectively isolated this area from the main accelerator vacuum. A Hall-Effect probe was incorporated for magnetic field measurements. Appropriate regulators and controllers were designed and constructed for the Hall probe and for the DC generator supplying the magnetic analyser. Energy calibration of the magnetic analyser was carried out. Improvements were made in the beam current integrator and in the optical periscope viewing system of the accelerator.

A stilbene crystal was used as the neutron detector, and appropriate electronic circuits were built for analysis of the pulse shapes obtained.

In parts II and III of this thesis, the experimental details are described. The results of the measurements are presented in part IV, and some of the astrophysical considerations relating to the $^{13}C(\alpha, n)^{16}O$ reaction are discussed in part V.

II. APPARATUS AND METHODS

(a) Alpha Beam

For the series of experiments described here the $^4He^+$ beam from the Kellogg Radiation Laboratory 700 kV Electrostatic accelerator was used. The machine uses an Oak Ridge type RF ion source, and has a maximum terminal voltage of about 700 kV. After passing through the steering magnets, the beam enters the 90^o analysing magnet. The analysed beam is collimated by regulating and beam-defining slits, and then passes through a long cold trap. This trap, a 1.5 cm diameter by 31 cm long tube completely immersed in liquid nitrogen, prevents condensible organic vapors from reaching the target area. The usual gate valves and pump-outs are available for isolating various sections of the beam tube. The rest of the beam-handling facilities are related to the target area, and will be described separately.

The maximum available beam measured on the target was 38 μa, and for the $^{13}C(\alpha,n)^{16}O$ experiment, beams of 25-30 μa were commonly used.

(b) Magnetic Analyser, Current Regulator, and Hall Probe

Momentum analysis of the accelerator beam was provided by a 41 cm 90^o double focusing analysing magnet. With a coil resistance of 0.3Ω, nearly 60 amperes are required to deflect a 0.700 MeV $^4He^+$ ion. For energy resolution of ± 0.5 keV, current stability of better than 1 part in 500 is required.

The magnet current regulating system employed was patterned after that described by Garwin (1959), using an 18-volt 200-ampere DC welding generator. In this system (see figs. 1-4), the magnet current flows through a Constantan shunt of very low resistance, and the voltage drop so produced is compared with a stable, adjustable reference, in this case a portion of the voltage across a mercury cell. Any error signal is converted to AC by means of a chopper, amplified, and re-converted to DC. The correction signal of the proper polarity is sent to a bank of 3 parallel-connected transistors in series with the magnet and generator (see fig. 2). The conductance of these pass transistors is thus modulated in such a way as to hold the current constant to better than 1 part in 10^4. In addition, a sensing circuit was designed (see fig. 3) which supplies only enough current to the generator field to provide a 1- or 2-volt drop across the transistors, plus the required voltage across the magnet. In this way the power dissipation of the pass transistors is kept to an absolute minimum.

The entire circuit is transistorized, with the exception of the first stage of the error amplifier. This is a high-gain DC chopper amplifier, modified from a commercial "Brown chopper amplifier". There are only two controls: an on-off switch, and a ten-turn potentiometer for adjusting the current. In nearly 3 years of operation the system has been stable and trouble-free.

The 3 pass transistors plus one driver transistor are mounted on a water-cooled copper heat sink. Safety precautions include a thermoswitch which opens the generator field if the cooling water is shut off, and Zener diodes protecting the pass transistors from transients and overvoltage. Current is divided

equally among the 3 transistors by the inclusion of 0.06Ω nichrome resistors in each emitter lead.

Magnetic field measurements are carried out by means of a Hall-Effect probe placed between the pole pieces of the magnet. Because of the very narrow gap, the installation of a more conventional NMR system was not attempted. This would have required the use of compensating coils to offset the $r^{-1/2}$ dependence of the magnetic field, making for too large a probe.

A Hall probe offers several advantages over an NMR system for magnetic field measurements. It is small and compact, and the output is a DC voltage. The disadvantages are its low output signal (tens of millivolts) and moderate temperature sensitivity. With the proper equipment, however, these two factors can be overcome to permit the desired degree of precision.

The Hall probe is a thin wafer of semiconducting material (in this case Indium Arsenide) with electrical contacts made at four edges. A constant control current is passed through two opposing contacts. Applying a magnetic field perpendicular to the face of the probe causes a potential difference to appear across the other two contacts. This potential difference, whose magnitude is proportional to the product of field and control current, is typically several hundred millivolts for a ten kilogauss field and several hundred milliamperes of control current. The device has a very low output impedance, and termination of the output by a resistor specified by the manufacturer gives the best linearity of response to applied magnetic field.

The device used in this application was the Siemens Field Probe SA 23. The manufacturer states that the mean temperature coefficient of the Hall voltage is -0.1%/deg C. between 0^{o} and 100^{o}C.

Room ambient temperature varies as much as five degrees over the year, and the temperature inside the magnet depends on the current being passed through it. Due to these variations, temperature compensation of the Hall probe was necessary in order to achieve the desired precision in the magnetic field measurements. A copper heat sink 6.4 x 2.5 x 1.3 cm was fashioned to completely enclose the probe. In addition, holes were provided for a 2000Ω glass-enclosed bead thermistor and a 47Ω carbon resistor. The thermistor serves as one arm of an AC-excited bridge, and the 47Ω resistor is the heating element. A simple transistor circuit (see fig. 5) supplies current pulses to the heater when the bridge is unbalanced, thus keeping the temperature of the copper block at a constant value. The normal operating temperature was chosen to be 42°C. Maintaining this temperature requires a steady DC input power of 0.3 watts. A sensitive mercury thermometer was inserted in the block to serve as a temperature monitor. Over a period of two years, the temperature has remained within ± 0.2°C. of the desired value. The temperature controller is operated continuously.

A very stable control current is required for precise field measurements. To this end a constant current source was designed and fabricated, utilizing a high-gain DC chopper amplifier in the feedback loop (see fig. 6). The rest of the circuit is transistorized. Hourly stability is better than 10 parts per million. A 2Ω manganin-wire resistor is used as the current sensing element, and a mercury cell as the reference voltage. The current is automatically held at a low value when the source is initially turned on. This is accomplished by the 100μf-470kΩ network at the input of the 2N1309

transistor. During this interval the chopper amplifier has time to warm up, and it then takes over and stabilizes the output current at 225 ma.

Typical values of Hall voltage, with a terminating resistor of 9Ω, range up to 100mv at the field required to bend a 0.765 MeV $^4He^+$ ion. A Rubicon potentiometer is used to measure the Hall voltage, with precision equal to ± 0.02%, or about ± 0.1 keV.

(c) Energy Calibration

Calibration of the 41 cm analysing magnet and Hall probe has been accomplished by means of resonances in the reactions $^{11}B(p,\gamma)^{12}C^*$ and $^{19}F(p,\alpha\gamma)^{16}O$. In the following table, the reaction, mass of bombarding particle, bombarding energy, resonance width, and gamma energy are given. In all cases the charge of the incoming particle is 1, and the energy per nucleon is the resonance energy.

	Reaction	Mass	E_B(MeV)	Γ(keV)	E_γ(MeV)
1)	$^{11}B(p,\gamma)^{12}C^*$	1	0.1631	6.3	11.68
2)	$^{19}F(p,\alpha\gamma)^{16}O$	1	0.3405	2.7	6-7
3)	$^{19}F(p,\alpha\gamma)^{16}O$	1	0.4836	1.8	6-7
4)	$^{11}B(p,\gamma)^{12}C^*$	2	0.3262	12.6	11.68
5)	$^{11}B(p,\gamma)^{12}C^*$	3	0.4893	18.9	11.68

The values of resonance energies and widths were taken from the article by Marion on accelerator energy calibration (1961).

The ^{11}B target was a pellet of separated ^{11}B isotope pressed into a stainless steel holder. It served as an infinitely thick target. The ^{19}F target consisted of a layer of CaF_2 evaporated onto a 0.005" Ta backing. Its thickness was approximately 7.5 keV to 0.480 MeV protons, essentially a thick target. Gamma rays were detected by a 2" x 2" NaI(Tl) scintillator, with a Hamner DDL amplifier serving as an integral discriminator, accepting all pulses with an energy greater than 3 MeV.

A computer program (CNDCAL) was written to accept the five values of Hall voltage (V_H) vs energy (E) and beam atomic number (A), and to fit these points by the method of least squares to a function of the form

$$V_H(\text{millivolts}) = V_0 + c(AE)^{1/2} + d(AE), \text{ with } E \text{ in keV.}$$

Each point was weighted according to the precision of measurement. When the parameters V_0, c, and d are obtained, V_H is calculated for beams of mass 1 to 4 and energy from 0.000 to 0.998 MeV in 0.002 MeV steps. In addition, the program computes the uncertainties in the coefficients V_0, c, and d.

Since the calibration points were derived from resonances of finite width, the weights were set equal to the inverse square of the width of the resonance involved.

The stability and reproducibility of the system has been shown to be excellent by repeated measurements of thick target excitation curves using ^{13}C targets. The reaction $^{13}C(p,\gamma)^{14}N$ has

a very sharp resonance at 0.4485 MeV (Vogl 1963), and every measurement made on this resonance has been within 0.5 keV of the correct value.

The presence of the offset term V_0 is due to the difficulty in placing the Hall voltage leads exactly opposite one another. An ohmic voltage drop is present with no magnetic field, caused by the flow of the control current. The term $c(AE)^{1/2}$ is what one would expect from the fact that the energy of the analysed particle varies with the square of the magnetic field. If the response of the Hall probe were linear with magnetic field, only these two terms should appear in the expression for V_H. The term $d(AE)$ represents non-linearity due to intrinsic limitations of the device itself and also changes in field shape as the field is increased. Because the Hall probe occupies a finite area in a region where the field is varying like $r^{-1/2}$, any changes in the field gradient caused by saturation effects will be reflected in the total integrated output of the device.

In the most recent calibration taken 1 month before the $^{13}C(\alpha, n)^{16}O$ experiment was run, the following values of V_0, c, and d were obtained: $V_0 = -0.545 \pm 0.169$, $c = 1.652 \pm 0.015$, and $d = 0.0032 \pm 0.0003$.

(d) Current Integration

Charge measurements were made with the 700 kV accelerator current integrator, considerably modified for these experiments. The original circuit is described in Wenzel's thesis (1952). A high-stability capacitor is charged to a predetermined voltage by the beam current. The voltage is read by a low-leakage

Acorn vacuum tube connected as a cathode follower. When the preset voltage is reached, the capacitor is discharged in a very short time, and the discharge is recorded on a counter. Thus the total charge is given by the product of the capacitance, the number of discharges, and the discharge voltage. In the present series of experiments a 0.944μf capacitor was charged to 98.6V. A 300V battery connected between target and current integrator provides secondary electron suppression. In addition, a 2MΩ resistor has been inserted in series with the current lead. A high impedance Field-Effect transistor voltmeter was designed to read the voltage across this resistor, and it drives a 25μa meter serving as a beam current indicator (see fig. 7). The usable range extends from 0.25 to 250μa full scale in seven ranges. Upstream from the target an electron suppressor ring completely surrounds but does not touch the beam. It is biased to -300V, and prevents any electrons produced in the beam tube from reaching the target.

(e) Target Chambers and Targets

Two types of target chamber were used in the experiments. For $^{13}C(\alpha,n)^{16}O$, where the yield is very low, a chamber permitting maximum solid angle in detection was used. In this case the target itself served as the end of the vacuum chamber, and the counter could be placed immediately adjoining the back face (see fig. 8). For $^{9}Be(\alpha,n)^{12}C$, chambers with cylindrical symmetry about a vertical axis were used, allowing angular distribution measurements to be made (see fig. 9). Since power dissipations in the 10 watt region were commonly encountered, all the chambers were force-cooled by an air blast. It was desirable to keep the targets themselves

at an elevated temperature to reduce carbon buildup. The chambers were cooled to preserve the vacuum seals. Both teflon and ungreased viton O-rings were used.

Immediately in front of the target and concentric with the beam was placed a long cold sleeve cooled to liquid nitrogen temperature (see fig. 8). The target volume, extending to the cold trap mentioned in section (a), was kept at high vacuum by a 9 liters/sec titanium-getter ion pump (manufactured by Ultek Corp.). Pressures read on the ion pump gauge during bombardment ranged from 3 to 4 x 10^{-7} torr. The precautions taken to keep the vacuum system free from organic vapors were necessary to hold the amount of carbon deposited on the targets to an absolute minimum. Pearson (1963) has found that the carbon deposition rate is proportional to the beam current and also to the target pressure. Any carbon buildup on the ^{13}C target would be especially noticeable because of the high beam currents and long bombardments. A natural carbon layer (1% ^{13}C) would reduce the energy of the particles incident on the ^{13}C layer, and thus reduce the neutron yield, since the yield is a very steep function of the bombarding energy. Periodic checks of the yield at 0.625 MeV showed that carbon deposition was not a problem.

Thick ^{13}C targets were made by heating 1/16" x 7/8" diameter copper discs to red heat in an atmosphere of ^{13}C-enriched methyl iodide vapor. The pressure used was about 10 cm of mercury. Methyl iodide (CH_3I) enriched to 54% in ^{13}C was obtained from Bio-Rad Laboratories, Richmond, Calif. As deduced from measurements made on a narrow resonance in the reaction $^{13}C(p,\gamma)^{14}N$, the targets had thicknesses near 0.200 MeV for 0.600 MeV alpha particles,

corresponding to about 200$\mu g/cm^2$ (see fig. 10 for typical thick target excitation curve).

Thin ^9Be targets were made by evaporating Be metal from tantalum boats onto clean polished 1/16" copper blanks. Target thicknesses were of the order of 25$\mu g/cm^2$, giving an energy loss of ~ 0.015 MeV for 0.600 MeV alpha particles.

Both the Be and C targets withstood long bombardments with little deterioration except for some discoloration.

(f) Stilbene Neutron Detector and Pulse-Shape Discriminator

Because of the low yields expected in the $^{13}C(\alpha, n)^{16}O$ reaction, it was necessary to choose a neutron detector possessing a very high efficiency. In addition, the detector chosen had to be insensitive to gamma rays. There are no gamma rays produced in $^{13}C(\alpha, n)^{16}O$, but a 4.43 MeV gamma ray accompanies each neutron in the $^9Be(\alpha, n_1)^{12}C^*(4.43)$ reaction. However, even room background exceeds the $^{13}C(\alpha, n)^{16}O$ count rate by several orders of magnitude at low bombarding energies, so gamma-ray elimination became a major consideration.

For these reasons a scintillation counter employing a stilbene crystal was chosen. In this type of detector the neutron undergoes n-p scattering, and it is actually the recoiling proton that is detected. Stilbene, an organic compound with chemical formula $C_{14}H_{12}$, is available only in small crystalline sizes, and the crystal used in these experiments was 1 1/2" in diameter by 1 1/2" long, mounted in an aluminum enclosure. If high efficiency alone were desired, a large plastic scintillator (main requirement: high percentage of hydrogen) could have been used. However,

stilbene possesses the additional characteristic of providing different pulse shapes for events due to electrons from those due to protons. This phenomenon was first noticed by Wright (1956), who measured the decay times of pulses from stilbene (see Appendix II). Since 1958, circuits have been published which enable efficient discrimination of neutrons over a wide range of energies. The discrimination circuit used here was developed by Daehnick and Sherr (1961), and all the subsequent analysis circuits were developed by the author (see block diagram of system, fig. 11).

The crystal was optically coupled by Dow Corning C-20057 Compound to a RCA type 6810A 2" photomultiplier tube. Layers of "Netic" and "Conetic" foil were wrapped around the assembly to provide shielding from stray magnetic fields. The tube anode voltage was 1940V, provided by a Fluke model 412B regulated power supply.

Included in the phototube base are an integrating-type preamplifier for the linear signal and the initial pulse-shape discrimination circuit (see fig. 12). The linear signal (L) passes on directly for further analysis, while the pulse-shape discrimination (PSD) pulse undergoes preliminary amplification and shaping in the phototube base. This PSD pulse (see Appendix II) is positive for protons, and its amplitude is roughly proportional to the corresponding linear signal of the proton recoil. It is delayed by 2 to 3μs with respect to the L pulse, a characteristic of the time constants and operating mode of the circuit. The discriminating circuit contains no active elements, and has three variable capacitors which are adjusted so that an electron produces zero or negative

output. Three stages of amplification, biased to clip negative pulses, ensure that only positive (proton) pulses are amplified and passed on for further analysis.

The circuits in the phototube base receive their power through the L signal lead. Both the L and PSD pulses are sent to the main electronics, where each event is subjected to various tests which determine whether it is an acceptable neutron event (see figs. 13-15). If so, it is stored in the pulse-height analyser, and also recorded in a decade scaler.

In order that an event be attributed to a neutron, several criteria must be satisfied. Firstly the L pulse must be above a preset minimum level. If this is the case, the lower level discriminator generates a 14μs "GO" pulse. Then both the L and PSD pulses are amplified and stretched. Each pulse stretcher produces a rectangular pulse whose amplitude equals that of the input and whose length is 14μs. Action of the stretchers is terminated by the falling edge of the GO pulse. Stretched L and PSD pulses are applied to the X and Y plates of an oscilloscope, for display purposes. In addition, the L pulse is sent to an upper level discriminator. If the amplitude exceeds the level set there, a "V" veto pulse is generated.

The second criterion which must be satisfied is that the amplitudes of the L and PSD pulses must bear a certain relation to one another. More specifically, the two stretched pulses are applied to the inputs of a differential amplifier. It computes the function (f · PSD - L), where f can be varied from 0 to 1. For a proton recoil, PSD is very closely proportional to L, whereas for an electron event PSD is very much smaller and is essentially

independent of L. If $|f \cdot PSD|$ is greater than $|L|$, the circuit allows a gate pulse "G" to be generated.

The final test that the event must pass is a time coincidence test. G and GO are fed to a coincidence mixer, along with V in anticoincidence. If G and GO appear simultaneously without the presence of V, the event is accepted as a neutron event. In this case a 7μs pulse is generated by the brightener trigger pair and applied to the Z axis of the display oscilloscope. This axis controls the intensity of the display. The timing of this pulse is such that it appears and disappears while the stretched pulses are still at their peak values. Thus an event appears on the oscilloscope as a brightened dot in the 2-dimensional L-PSD field. All proton recoils fall on a diagonal line. Electron events also appear, but their traces are not intensified, and they fall entirely on the X axis. If desired, the oscilloscope intensity control can be adjusted to make electron events just barely visible or completely invisible.

After an event has been accepted, a coincidence pulse "C" is generated to be used in the Delayed Coincidence input of a RIDL 34-12 400-channel pulse-height analyser. The L pulse is suitably amplified and passed through a 0.8μs delay line, in order that the timing relations be correct. Positive outputs are provided to record the GO and C pulses on decade scalers.

Adjustment of the circuit is extremely simple with the help of the display oscilloscope. The intensity is turned up so that both electron and proton events are visible when the counter is exposed to a source of neutrons and gamma rays. The count rate should not be in excess of several thousand counts/sec. Variable capacitors R, C, and F are adjusted so that the proton recoil locus is separated from the electron locus as much as possible. The best setting will be

clearly seen if the count rate is high enough to provide a continuous display of events.

During the course of runs with $^{13}C(\alpha, n)^{16}O$ it was discovered that sparks causing minor fluctuations in the accelerator terminal voltage were registering as events, which could not be discriminated from neutrons. Efforts were made to shield out this RF energy, but they were unsuccessful. The reason for this is clear when one considers that the energy had to penetrate the thick grounded pressure tank of the accelerator. It must be a very low impedance source indeed! However, these fluctuations could be detected as sudden changes in the column current flowing down the bleeder chain resistors. Accordingly a circuit was devised which produced a V pulse only upon the appearance of a very fast transient on the resistor column current (see figs. 16 and 17). The timing of the pulses is such that the V pulse arrives in time to cancel an event due to a machine spark. These fluctuations were random in nature, sometimes occurring every few minutes and sometimes not at all.

In order to check the efficiency of the spark detector, the C scaler pulse was connected to a beeping device, also audible in Room 101 Kellogg. Every time an event was registered, the audio tone thus produced could be correlated with any fluctuation appearing in the column current. The spark detector worked well enough to relieve the author of having to continuously watch for such spurious events on the column current meter.

With the variable upper and lower thresholds, and the variable L/PSD ratio, the circuit is effective in eliminating about 99.97% of all gamma rays, while counting proton recoils down to an energy of 0.9 MeV (see figs. 18 and 20). The gamma-ray elimination can be improved by raising the lower level of

discrimination to 1.25 MeV, at which point about 7 counts per hour were recorded as background, all at low energy. In fact, this was the lower level setting used in the $^{13}C(\alpha,n)^{16}O$ experiment.

At higher count rates the circuit performance is slightly degraded. Because of the dead time of the GO trigger circuit, charge tends to pile up on the pulse stretchers if pulses come at less than 14μs intervals. A reasonable count rate is 5000 counts/sec.

(g) Detector Efficiencies and Yield Calculations

It is a fairly straightforward procedure to calculate the detection efficiency of a neutron counter such as is described above, for a parallel beam of incident neutrons. The neutrons scatter off hydrogen and carbon, but it is only the proton recoils that produce a scintillation large enough to elicit a response at the photocathode. Due to scattering, the beam of incident neutrons is attenuated on passing through the crystal. These considerations can be expressed mathematically in terms of the n-p scattering cross-section and the n-carbon total cross-section.

However, in the present experiment, the beam of neutrons cannot be considered to be parallel. Angular factors must be employed when calculating the efficiency, because the path length in the crystal is a function of the angle of incidence of the neutron. In addition, the neutron energy depends on the angle of incidence, and thus the n-p scattering cross-section is different for every angle.

Another consideration is the fact that only protons whose energies lie above the lower level discriminator setting are accepted for analysis. In Appendix I it is shown that the energy distribution

of proton recoils from a neutron beam of energy E_n is of the form:

$$\frac{dN_p}{dE_p} = \begin{cases} \text{constant for } 0 < E_p \leq E_n \\ 0 \text{ for all other } E_p \end{cases} .$$

This means that if the number of proton recoils between some cutoff energy E_{c0} and the maximum energy E_n is known, the total number of protons is given by that number multiplied by the factor $E_n/(E_n-E_{c0})$. It is only necessary to know the energy E_{c0} corresponding to the cutoff channel chosen in the pulse-height spectrum, to be able to determine the true number of proton recoils from zero energy to E_n. Since this factor is a function of neutron energy as well, it must be included in the efficiency calculation for each angle of incidence.

In practice, all the above mentioned effects are included in one integral, and the integration is carried out over the geometry of the crystal. A computer program has been written which produces the detector efficiency, including the solid angle, as a function of target nucleus, bombarding particle, crystal dimensions, angle made by crystal axis with the beam direction, target-to-detector distance, and low-energy cutoff. The integration is done numerically on the IBM 7094 computer. Provision is also made for inserting corrections due to absorption by the target backing.

(1) Yield of $^{13}C(\alpha, n)^{16}O$

This reaction has an extremely low yield at low energies, so that to determine the total cross-section by conventional methods is impossible, i.e. thin target excitation functions and angular distributions. Several crude angular distributions using moderately thick targets were measured and showed that an assumption of isotropy was consistent within about 25 percent. Thus the total cross-section could be obtained from the 0^{o} yield, measured with as great a solid angle as possible. The front face of the counter was placed 3 mm from the front face of the target (see fig. 19). A thick target ($\sim 200 \mu g/cm^2$) was used, and the yield of neutrons was measured at bombarding energies from 0.475 to 0.700 MeV in 0.025 MeV steps. As it turned out, the yield essentially doubled every 0.025 MeV. For a thick target, containing ^{13}C and ^{12}C, the yield is given by

$$Y(E_B) = \left(\frac{nCV}{q}\right) \cdot p \cdot \int_{E_B - \varepsilon_T}^{E_B} \frac{\zeta(E_L)\sigma(E_L)dE_L}{\epsilon(E_L)}$$

where

$Y(E_B)$ is yield at alpha-particle bombarding energy E_B, in the laboratory system

$\frac{nCV}{q}$ is number of incident alpha-particles

n is number of current-integrator discharges

C	is current-integrator capacitance = 0.944μf
V	is current-integrator discharge voltage = 98.6V
q	is charge per incident alpha-particle = 1.6×10^{-19} coulomb
p	is fraction of target which is ^{13}C = 0.545
E_L	is alpha-particle energy in MeV in the laboratory system
$\zeta(E_L)$	is efficiency of counter for isotropic source including solid angle factor
$\sigma(E_L)$	is total cross-section at energy E_L in barns
$\epsilon(E_L)$	is stopping cross-section for ^4He beam particles in carbon at energy E_L in MeV-barns
ε_T	is target thickness in MeV in laboratory system $\geq$ 0.200 MeV.

The efficiency $\zeta(E_L)$ is obtained from the following integral:

$$\zeta(E_L) = \frac{1}{4\pi} \int_0^{2\pi} d\varphi \int_{\text{crystal}} (A)(B)(C)(D)\sin\theta\, d\theta \qquad (2)$$

where

$$A = \exp(-x'(\theta) \cdot n_{Cu}\sigma_{Cu}) = \exp(-0.047\sec\theta)$$

$$B = \frac{n_H \sigma_H}{n_H\sigma_H + n_C\sigma_C}$$

$$C = 1 - \exp\left[-x(\theta) \cdot (n_H \sigma_H + n_C \sigma_C)\right]$$

$$D = 1 - \frac{1.25}{E_n}$$

and

$n_H \sigma_H$ is number of H atoms in stilbene/cm^3 x n-p scattering cross-section

$n_C \sigma_C$ is number of C atoms/cm^3 x total neutron cross-section for carbon

$n_{Cu} \sigma_{Cu}$ is number of Cu atoms/cm^3 x total neutron cross-section for copper

$x(\theta)$ is path length for neutron in stilbene crystal (see fig. 19)

$x'(\theta)$ is path length for neutron in target backing

E_n is neutron energy in MeV in laboratory system $= E_n(E_L, \theta)$.

Both $n_H \sigma_H$ and $n_C \sigma_C$ are functions of neutron energy E_n. Term A accounts for the absorptive effect of the copper target backing. Term B gives the fraction of neutron interactions in the crystal which lead to a detectable recoil proton. Assuming that any interaction whatever removes a neutron from the beam, term C describes the attenuation of the beam in passing through the crystal. Finally, term D provides the fraction of proton recoils accepted, due to their

energies being greater than the lower level discriminator threshold, set in this case at 1.25 MeV.

The integral over φ can be evaluated, since there is cylindrical symmetry about the crystal axis. Then the yield is given by

$$Y(E_B) = 1.59n \cdot 10^{14} \int_{E_B - \varepsilon_T}^{E_B} \frac{I_\zeta(E_L)\sigma(E_L)dE_L}{\varepsilon(E_L)}$$

where

$$I_\zeta(E_L) = 2\zeta(E_L) .$$

$I_\zeta(E_L)$ is a slowly varying function of E_L, ranging from 0.0733 at 0.4875 MeV to 0.0751 at 0.6875 MeV.

Since a low-energy nuclear reaction is involved, the substitution

$$\sigma(E_L) = \frac{S(E_L)\exp(-2\pi\eta)}{E_L} \quad \text{is useful.} \tag{3}$$

Then

$$Y(E_B) = 1.59n \cdot 10^{14} \int_{E_B - \varepsilon_T}^{E_B} \frac{I_\zeta(E_L)S(E_L)\exp[-23.75/(E_L)^{1/2}]dE_L}{E_L\varepsilon(E_L)} \tag{4}$$

where $S(E_L)$ is the astrophysical cross-section factor introduced in equation (1), page 2. Its units are MeV-barns, in the laboratory system.

The evaluation of equation (4) to obtain $S(E_L)$ is best accomplished by substituting expressions for $I_\zeta(E_L)$ and $\epsilon(E_L)$, and postulating a functional form for S. Since $I_\zeta(E_L)$ and $\epsilon(E_L)$ are slowly varying with E_L, power series expansions up to terms in E_L^2 are sufficient. Differentiation of the yield curve showed that $S(E_L)$ was well represented by a two-term linear function

$$S(E_L) = S_L(0) + \alpha E_L$$

where $S_L(0)$ and α are unknown constants. Also required for the integral is the target thickness ϵ_T. However, the exponential term so dominates the integrand that less than 1% of the integral is due to energies more than 0.200 MeV below E_B. The target is thicker than 0.200 MeV in all cases. Using 0.300 MeV as a suitable thickness,

$$Y(E_B) = 1.59n \cdot 10^{14}\left\{S_L(0)\int_{E_B-.300}^{E_B}\frac{I_\zeta(E_L)\exp[-23.75/(E_L)^{1/2}]\,dE_L}{E_L\,\epsilon(E_L)}\right.$$

$$\left. + \alpha\int_{E_B-.300}^{E_B}\frac{I_\zeta(E_L)\exp[-23.75/(E_L)^{1/2}]\,dE_L}{\epsilon(E_L)}\right\}$$

$$= 1.59n \cdot 10^{14}\,[S_L(0)I_1 + \alpha I_2] \quad .$$

The stopping cross-section $\epsilon(E_L)$ has been taken from Porat and Ramavataram (1961), who state the precision of their absolute measurements to be 5%. Integrals I_1 and I_2 have been performed on the IBM 7094 computer, and are found in Table 1.

The constants $S_L(0)$ and α are found from a least-squares fit of all the yields taken at the various bombarding energies. Errors used in this fit are the statistical uncertainties in the yields. Other uncertainties are applied to the final answers.

To convert the value of $S(E_L)$ from the laboratory to the center-of-mass system, we notice that the ratio $S(E)/E$ is the same in both systems (see equation (3)). Thus

$$S(E) = \frac{E}{E_L} [S_L(0) + \alpha E_L]$$

$$= 0.76464 S_L(0) + \alpha E \quad \text{MeV-barns, CM system} \qquad (5)$$

where the coefficient α is unchanged since $S(E)/S(E_L) = E/E_L$.

(2) Yields of $^{9}Be(\alpha, n_0)^{12}C$ and $^{9}Be(\alpha, n_1)^{12}C^*(4.43)$

These reactions have a significantly higher yield than the $^{13}C(\alpha, n)^{16}O$ reaction, so thin target excitation functions and angular distributions were measured. Both neutron groups are present in the pulse-height spectrum, and they can be separated to obtain differential cross-sections (see fig. 20). The procedure is as follows: A cutoff energy E_{c0} is chosen (refer to fig. 20) such that only ground-state neutrons are present above it. The counts are

summed from there up to an energy which is definitely higher than the energy of the group. Let this sum be Σ_0. If N_0 is the number of ground-state neutrons emitted into 4π if the source were isotropic, then

$$\Sigma_0 = \frac{N_0}{4\pi} \int_{\text{crystal}} f(\Omega) \left[1 - \frac{E_{c0}}{\bar{E}_{n0}} \right] d\Omega = \frac{N_0}{4\pi} I_0$$

where

$f(\Omega) = (A)(B)(C)$ as defined in section (g), (1), part II, except that the variable θ is replaced by a dependence on the φ-direction in the crystal and the angle made by the crystal axis with the beam direction.

The target-backing correction term (A) is used only when the backing comes between the target surface and the counter.

Next a lower cutoff energy E_{c1} is chosen such that it is slightly above the lower level discriminator bias. The counts between this cutoff energy E_{c1} and the upper cutoff E_{c0} are summed. Included here are both ground- and first excited-state neutrons. Let this sum be Σ_1, and let the number of ground-state neutrons contained in Σ_1 be Σ_2. But

$$\Sigma_2 = \frac{N_0}{4\pi} \int_{\text{crystal}} f(\Omega) \left[\frac{E_{c0} - E_{c1}}{E_{n0}} \right] d\Omega$$

$$= \frac{N_0}{4\pi} \int_{\text{crystal}} f(\Omega) \left[\left(1 - \frac{E_{c1}}{E_{n0}}\right) - \left(1 - \frac{E_{c0}}{E_{n0}}\right) \right] d\Omega$$

$$= \frac{N_0}{4\pi} (I_2 - I_0)$$

where

$$I_2 = \int_{\text{crystal}} f(\Omega) \left[1 - \frac{E_{c1}}{E_{n0}} \right] d\Omega \ .$$

Subtracting Σ_2 from Σ_1 gives the number of first excited-state neutrons in the energy interval $(E_{c0} - E_{c1})$, or equivalently, the number of first excited-state neutrons between the lower energy cutoff E_{c1} and the maximum neutron group energy E_{n1}. Let this number be Σ_1' .

$$\Sigma_1' = \frac{N_1}{4\pi} \int_{\text{crystal}} f(\Omega) \left[1 - \frac{E_{c1}}{E_{n1}} \right] d\Omega = \frac{N_1}{4\pi} I_1$$

where N_1 is the number of first excited-states neutrons emitted into 4π if the source were isotropic.

We have

$$\Sigma_1' = \Sigma_1 - \frac{N_0}{4\pi} (I_2 - I_1) \ .$$

But

$$\frac{N_0}{4\pi} = \frac{\Sigma_0}{I_0} \text{ , so } \frac{N_1}{4\pi} = \frac{\Sigma_1 - \frac{\Sigma_0}{I_0}(I_2 - I_0)}{I_1} \text{ .}$$

The quantities of interest are $N_0/4\pi$ and $N_1/4\pi$, which are related to the differential cross-sections at the angles concerned. From the known stopping cross-section of ^{4}He particles in Be (Whaling 1958) and the measured width of a very narrow resonance obtained from the excitation function (see fig. 24), the target thickness was obtained. This was found to be $(0.514 \pm 0.037) \times 10^{18}$ atoms/cm^2. So

$$\frac{N}{4\pi} = \left(\frac{d\sigma}{d\Omega}\right) \times \text{(number of incident particles)} \times \text{(thickness)}$$

in appropriate units. Putting in the correct constants, we obtain

$$\left(\frac{d\sigma}{d\Omega}\right) = \frac{0.00335}{n} \left(\frac{N}{4\pi}\right)$$

where n is the number of integrator discharges.

Finally

$$\left(\frac{d\sigma}{d\Omega}\right)_{n_0} = \frac{1}{299n} \left(\frac{\Sigma_0}{I_0}\right) \frac{\mu b}{sr} \text{ , laboratory system}$$

$$\left(\frac{d\sigma}{d\Omega}\right)_{n_1} = \frac{1}{299n} \frac{\Sigma_1 - \frac{\Sigma_0}{I_0}(I_2 - I_0)}{I_1} \frac{\mu b}{sr} \text{ , laboratory system.}$$

The integrals I_0, I_1, and I_2 have been calculated numerically on the IBM 7094 computer.

III. EXPERIMENTAL PROCEDURE

(a) $^{13}C(\alpha, n)^{16}O$

Before performing any runs on the $^{13}C(\alpha, n)^{16}O$ reaction it was necessary to establish an energy calibration for the stilbene neutron counter. This enabled the lower level discriminator to be set at 1.25 MeV, the value selected as giving good detection efficiency combined with a low background count. The calibration was carried out using the reaction $^{9}Be(\alpha, n)^{12}C$ at three different energies: 0.4, 0.5, and 0.6 MeV. Before the runs, the equipment was allowed to warm up for 24 hours.

Supplementing the neutron energies as calibrations, three gamma rays were used as independent checks on linearity and gain. They were ^{137}Cs (0.66 MeV), and ^{22}Na (0.51 and 1.28 MeV). Since stilbene is an organic material, with very low-Z constituents (carbon and hydrogen), its response to low-energy gamma rays is entirely due to Compton scattering. The gamma rays were also used for recalibration purposes at a later data, allowing the overall gain to be reset at the $^{9}Be(\alpha, n)^{12}C$ calibration value. Gain stability over a day's run was found to be excellent, and with the low yields encountered, gain shifts due to count-rate were nonexistent.

Before each day's run, the linearity and zero level of the RIDL model 34-12 400-channel pulse-height analyser were checked using a mercury pulser, which was provided with a motorized amplitude control. This allowed the amplitude to be raised or lowered at a linear rate with time. Establishment of the zero level to within one channel was important, since zero volts = zero channel

was used as one of the energy calibration points. The internal amplifier of the RIDL was not used, but instead the pulses from the previously described electronics were fed directly to the analogue-to-digital converter by means of the DIRECT CONV input. Coincidence gate pulses (C) were applied to the DELAYED COINCIDENCE input. Each run was recorded in 100-channel segments, and the number of coincidence pulses was recorded on two separate decade scalers connected in parallel. The runs were terminated after approximately 20,000 μC of charge had been accumulated on the current integrator.

At regular intervals during the running day, a check was made on the condition of the target. This was accomplished by measuring the yield of the reaction at 0.625 MeV bombarding energy. Approximately 475 counts were obtained for 20,000 μC, the time taken being about 12 minutes. Any deposit of carbon caused by the bombardment would have shown up in the yield, since the energy of the incident particles would have been slightly degraded upon passing through the carbon layer. This layer contains only 1% ^{13}C, so there will be negligible contribution to the neutron yield. During the entire 16-hour bombarding period, no deviation in the yield at 0.625 MeV outside the statistics was noticed. As mentioned previously, target area pressure was 4×10^{-7} torr, and both liquid nitrogen traps were kept constantly filled during the run.

Half-way through the running day the beam was removed from the target and a background run was taken. Bombarding energy was set at 0.475 MeV. One count was observed in 1,000 seconds.

Beam current on the target varied throughout the running period from 20 - 27 μa. Air blast cooling was used on the target chamber, and was adjusted such that the target was visibly reddish in color under bombardment. This heating of the target by the beam helped to keep the deposition of contaminants at a very low level.

The thick target neutron yield for the $^{13}C(\alpha, n)^{16}O$ reaction was measured in 0.025-MeV steps from 0.475 MeV to 0.700 MeV. Data used for analysis were the scaler counts, with the pulse-height spectra used only as stand-by. At bombarding energies below 0.625 MeV, the runs were sufficiently long and the count-rate sufficiently low that background corrections were made, based on the length of the run. Above this energy the background was negligible. In fact, at the higher energies the statistics were good enough to allow less charge to be accumulated for each run. The total charge registered for the running period was 1.3 coulombs.

(b) $^{9}Be(\alpha, n)^{12}C$

The presence of two neutron groups in this reaction made energy calibration of the counter a routine matter. Before each day's run began, the same precautions and checks on the apparatus that were performed for the $^{13}C(\alpha, n)^{16}O$ were repeated for $^{9}Be(\alpha, n)^{16}O$. Because of the higher count-rates encountered, a lower level discriminator setting of 0.9 MeV could be tolerated, allowing a larger fraction of the low-energy first excited-state neutron group to be detected. All data analysis was performed on the pulse-height spectra, with the scaler counts serving as a monitor during the experiment.

Excitation functions were recorded at 0^{o} and 90^{o} in the laboratory system, between the energies of 0.340 and 0.680 MeV. The charge accumulated for the majority of the runs was 2,000 μC. A 4.5 cm diameter brass target chamber was used (see fig. 9), and the front face of the detector was 2.3 cm from the target center. In this position the front face of the detector subtended an angle of just under 40^{o} at the target.

In addition to the excitation functions, angular distributions were measured at 0.480, 0.520, 0.5925, and 0.608 MeV. In this case a stainless steel target chamber of diameter 2.5 cm was used, and the front face of the detector was placed at a distance of 8.1 cm from the center of the target. Data were taken at nine angles: 0, 20, 40, 60, 80, 100, 120, and 140 degrees in the laboratory system. During these runs, taken about 1 1/2 months after the excitation functions, the zero level of the RIDL 400-channel pulse-height analyser was malfunctioning, and a shift of nearly 10 channels was observed over the course of the running period. Corrections to each run have been applied to remove this shift, based on the mercury-pulser calibration made at the beginning of the running day.

An angle of just under 14^{o} was subtended by the front face of the counter at the target, permitting good angular resolution. The target was placed with its outward normal at an angle of -135^{o} to the incident beam direction. Angles below 90^{o} thus required a target-backing correction, while those greater than 80^{o} did not. The angle 80^{o} was measured under both conditions, in order to supply a check for the correction. For these measurements a beam current of 12 μa was used.

At the same time, two spectra were taken with reduced photomultiplier voltage and amplifier gain, in order to demonstrate the effect of the neutron-gamma discriminator. These spectra clearly show that the 4.43 MeV gamma ray from the decay of the first excited state of ^{12}C does not appear when the neutron-gamma discriminator is operating (see fig. 18).

The same target that was used for the excitation functions was used in the angular distribution measurements. The spark detector veto circuit was not used in any of the $^{9}Be(\alpha, n)^{12}C$ runs.

IV. RESULTS

(a) $^{13}C(\alpha,n)^{16}O$

The thick target neutron yield for the reaction $^{13}C(\alpha,n)^{16}O$ is shown in fig. 21, in counts per 20,000 μC. The observed numbers are found in Table 1. Along with the normalized experimental points is a solid curve computed from the least-squares fit to the yield. The results from this fit give $S_L(0) = (7.165 \pm 2.118) \times 10^5$ MeV-barns, and $\alpha = (12.047 \pm 3.623) \times 10^5$ MeV-barns. Uncertainties are due solely to the statistics. Equation (5) enables S(E) to be calculated, and this function appears in fig. 22, along with the stellar temperature scale associated with the center-of-mass energies. These are given in units of 10^8 ^oK (T_8). Knowing S(E), the total cross-section $\sigma(E)$ can be calculated, and this is shown in fig. 23. Also found in Table 1 are the calculated values of the yield and of the total cross-section at each energy point.

Before stating a final value for S(E), the sources of uncertainty must be considered. Besides the statistics, there exist uncertainties in the number of incident particles, the stopping cross-section $\varepsilon(E_L)$, and the efficiency integral $I_\zeta(E_L)$. An error of $\pm$ 5% can be assigned to the number of incident particles determined from the current integration. The stopping cross-section has an uncertainty of $\pm$ 5%. Systematic errors appear in the efficiency integral $I_\zeta(E_L)$. These are due to uncertainties in the crystal dimensions, detector-to-target distance, beam spot size and centering, as well as errors in determining the lower cutoff energy 1.25 MeV, and small errors in the n-p and n-carbon cross-sections. These latter quantities were

obtained from "Neutron Cross-Sections" (Hughes 1958), and were fitted to simple functions in the energy range concerned, in order that the calculations be done entirely by computer. From all of these factors, an uncertainty of 10% is assigned to the quantity $I_{\zeta}(E_L)$.

The total uncertainty in the final expression for S(E) is thus:

least-squares fit (statistics)	$\leq$ 30%	(see p. 101)
current integration	5%	
stopping cross-section	5%	
efficiency integral	10%	
Total	$\leq$ 32%	(see p. 101)

So

$$S(E) = [(5.48 \pm 1.77) + (12.05 \pm 3.91)E] \times 10^5 \text{ MeV-barns.}$$

If E is measured in keV the expression becomes

$$S(E) = [(5.48 \pm 1.77) + (0.012 \pm 0.004)E] \times 10^8 \text{ keV-barns.}$$

(b) $^9Be(\alpha, n)^{12}C$

On figures 24 and 25 are found the excitation functions for the ground- and first excited-state neutrons from the $^9Be(\alpha, n)^{12}C$ reaction, taken at 0^o and 90^o in the laboratory system. The yield has been converted to a differential cross-section by the method

outlined in Section (g)(2), part II.

Angular distributions for both neutron groups are shown in figs. 26 and 27. The experimental points have been fitted by the method of least squares to combinations of Legendre polynomials, and normalized to the calculated value at 90^{o}. All distributions are in the center-of-mass system. Terms up to and including $P_4(\cos\theta)$ were used when necessary.

Table 2 gives the coefficients found for each Legendre polynomial, normalized to the coefficient of $P_0(\cos\theta)$ taken equal to 1. The four bombarding energies at which angular distributions were taken were 0.480, 0.520, 0.593, and 0.608 MeV.

From the excitation function measurements the lower resonance at 0.520 MeV bombarding energy (11.01 MeV state in ^{13}C) is seen to have a laboratory width of 80 keV. The upper resonance at 0.600 MeV (11.08 MeV state in ^{13}C) can be assigned a laboratory width of less than 5 keV. A very thin Be target is required to further investigate the properties of this level.

An analysis of the experimental excitation functions and angular distributions by an R-matrix calculation is in principle feasible. However, as is obvious by the shape of the excitation functions, more than two levels are involved. In fact, the two broad states in ^{13}C at 11.97 MeV [$J^{\pi} = (7/2)^{-}$] and 12.87 MeV [$J > (5/2)$] are almost certainly affecting the data in the energy range measured. In view of the unknown characters of these upper states, and in the limited interest in the lower states in ^{13}C, it was decided not to pursue the calculation.

In the energy range studied, the reaction $^{9}Be(\alpha, n)^{12}C$ appears to populate equally the ground- and first excited-states of ^{12}C. An

uncertainty of about ± 15% can be assigned to the absolute differential cross-sections. Relative errors in the angular distributions are of the order of ± 5%. For further discussion of the resonance parameters applied to the $^{9}Be(\alpha, n)^{12}C$ reaction in a star, see the following section on astrophysical applications.

V. APPLICATIONS TO ASTROPHYSICS

Once experimental cross-section data are available for a thermonuclear reaction, it is useful to present the information in a format which enables the computation of variables of interest in astrophysics. A recent review article (Fowler et al 1967, henceforth referred to as FCZ) presents a compilation of experimental results from many thermonuclear reactions, and provides a series of numerical coefficients with which the reader may construct quantities pertinent to nuclear astrophysics. These are the reaction rates, nuclear lifetimes, and energy generation rates, as a function of stellar parameters like temperature, density, and abundances of the constituent nuclei. Two types of reactions are dealt with: those involving resonances in the compound state, usually occurring at stellar temperatures greater than 2×10^8 °K, and those exhibiting a slowly-varying non-resonant behavior with energy, typical of stellar temperatures below about 10^8 °K.

For the present application of the $^{13}C(\alpha, n)^{16}O$ reaction, we are concerned only with the non-resonant region, which in this case extends from T_9 ($T = 10^9$ °K) = 0 to 1. A short summary of the notation in FCZ will be in order.

The reaction rate between two nuclei 0 and 1 is given by

$$P_{01} = n_0 n_1 \langle 01 \rangle \text{ reactions-cm}^{-3}\text{-sec}^{-1}$$

where $\langle 01 \rangle \equiv \langle \sigma v \rangle$ in $\text{cm}^3\text{-sec}^{-1}$ is the product of cross-section and velocity averaged over the velocity distribution. The particle number densities are given by n_0 and n_1 in cm^{-3}. If the atomic abundances by mass X_0 and X_1 are used, $n_0 = \rho N_A X_0 / A_0$ and

$n_1 = \rho N_A X_1/A_1$, where ρ = matter density in gm-cm^{-3}, N_A = Avogadro's number, and A_0 and A_1 are the atomic mass numbers of 0 and 1. With respect to the laboratory, A_0 is the target nucleus and A_1 is the projectile.

The mean lifetime of the nucleus 0 for interaction with nucleus 1 is

$$\frac{1}{\tau_1(0)} = \lambda_1(0) = -\frac{1}{n_0}\frac{dn_0}{dt} = n_1\langle 01\rangle = \frac{X_1}{A_1}[01]\ \text{sec}^{-1}$$

where $$[01] = \rho N_A \langle 01\rangle\ \text{sec}^{-1}$$

so $$P_{01} = \rho N_A \frac{X_0 X_1}{A_0 A_1}[01]\ .$$

Energy generation by the exoergic reaction $0 + 1 \rightarrow 2 + 3 + Q$ is given by

$$\varepsilon_{01} = \frac{P_{01}}{\rho}\ Q(\text{erg})$$

$$= 9.6487 \times 10^{17}\frac{X_0 X_1}{A_0 A_1}[01]\ Q_6\ \text{erg-gm}^{-1}\text{-sec}^{-1}$$

where Q_6 is the reaction Q in MeV.

Before the previous quantities can be calculated, $\langle \sigma v \rangle$ must be determined. With the expression for $\sigma(E)$ given in equation (1) page 2, and using a Maxwellian velocity distribution, we obtain for charged particles

$$[01] = \left\{7.8327 \times 10^{9}(Z_0 Z_1/A)^{1/3} S(0)\right\} \frac{S_{eff}}{S(0)} \rho T_9^{-2/3} \exp(-\tau) \ .$$

The reduced mass number A is given by $A = A_0 A_1/(A_0 + A_1)$, and the factor in curly brackets is the numerical coefficient listed in Table III of FCZ. The quantity $S_{eff}/S(0)$ is a function of temperature:

$$\frac{S_{eff}}{S(0)} = 1 + (a)T_9^{1/3} + (b)T_9^{2/3} + (c)T_9 + (d)T_9^{4/3} + (e)T_9^{5/3} \ .$$

Coefficients (a) - (e) for the various powers of T_9 are given in FCZ, Table III, as is the quantity $\tau T_9^{1/3}$. For the lifetime,

$$\frac{1}{\tau_1(0)} = \left\{7.8327 \times 10^{9}(Z_0 Z_1/A)^{1/3} \frac{S(0)}{A_1}\right\} \frac{S_{eff}}{S(0)} X_1 \rho T_9^{-2/3} \times \exp(-\tau)$$

and the energy generation

$$\varepsilon_{01} = \left\{9.6487 \times 10^{17} \times 7.8327 \times 10^{9}(Z_0 Z_1/A)^{1/3} \frac{S(0)}{A_0 A_1} Q_6\right\}$$

$$\times \frac{S_{eff}}{S(0)} X_0 X_1 \rho T_9^{-2/3} \exp(-\tau) \ .$$

In the case of the $^{9}Be(\alpha,n)^{12}C$ reaction, it may be important in high temperature-high density situations where the primary constituents are alpha-particles and neutrons. In analogy to the 3-α process, some ^{9}Be could be produced in equilibrium quantities, forming ^{12}C via $^{9}Be(\alpha,n)^{12}C$. In a normal star, any ^{9}Be that is produced is quickly consumed by the reaction $^{9}Be(p,d)^{8}Be \rightarrow 2\alpha$. Several resonances exist in the $T_9 = 1$ region for $^{9}Be(\alpha,n)^{12}C$, and the parameters needed to compute the astrophysical lifetime of ^{9}Be can be obtained from the experimental data.

FCZ give, for a resonance at E_r in the center-of-mass system,

$$[01] = \left\{1.540 \times 10^{11} A^{-3/2} (\omega\gamma)_r\right\} \rho T_9^{-3/2} \exp(-E_r/kT) \text{sec}^{-1}$$

where

$$(\omega\gamma)_r = \left(\frac{\omega\Gamma_1\Gamma_2}{\Gamma}\right)_r \text{ MeV}$$

$$\omega = (2J_r + 1)/(2J_0 + 1)(2J_1 + 1) .$$

The J's are the spins of the resonant state, target nucleus, and projectile, while the Γ's are the widths associated with the Breit-Wigner cross-section (see FCZ). Two methods for obtaining $(\omega\gamma)_r$ are given by FCZ: one for "poor" resolution experiments, and one for "good" resolution experiments, where the quantities E_r, σ_r, and Γ_r are obtained from the experimental measurements. For the first case we have

$$(\omega\gamma)_r = \frac{2}{\pi} \cdot 3807(AE_r) \int_r \sigma dE \quad \text{center-of-mass system}$$

$$= \frac{2}{\pi} \cdot 3807\left(\frac{A_0}{A_0 + A_1}\right)^3 A_1(E_r)_L \int_r \sigma dE_L \cdot$$

In the second case,

$$(\omega\gamma)_r = .3807\left(\frac{A_0}{A_0 + A_1}\right)^3 A_1(\Gamma_r E_r)_L \sigma_r \text{ center-of-mass system.}$$

Referring to figs. 26 and 27, the total cross-section can be obtained from the 90^o excitation function with little error, because the average of each angular distribution is approximately the differential cross-section at 90^o. Because of the high neutron energies involved, conversion to center-of-mass angle from the lab angle of 90^o introduces negligible error. Taking the area under the yield curve for the narrow resonance yields for the two neutron groups:

$(\omega\gamma)_r = 0.51 \times 10^{-6}$ MeV (CM) ground-state group

$(\omega\gamma)_r = 0.37 \times 10^{-6}$ MeV (CM) first excited-state group.

For the lower, broader resonance the parameters are:

$E_r = 0.520$ MeV (LAB) $\quad E_r = 0.360$ MeV (CM)

$\sigma_r = 92\ \mu b$ ground-state group

$\sigma_r = 89\ \mu b$ first excited-state group

$\Gamma_r = 0.080$ MeV (LAB) $\Gamma_r = 0.055$ MeV (CM).

Adding the cross-sections for both groups, we obtain

$$(\omega\gamma)_r = 3.79 \times 10^{-6} \text{ MeV (CM)}.$$

The lifetime of the ^{9}Be nucleus to interaction with ^{4}He via $^9\text{Be}(\alpha, n)^{16}\text{O}$ may now be computed. Using numerical coefficients given in FCZ, including $(E_r/k)_9$ (degrees $\times 10^9$), the result is

$$\frac{1}{\tau_{^4\text{He}}(^9\text{Be})} = \frac{1}{3.17 \times 10^{-5}} X_{^4\text{He}} \rho T_9^{-3/2} \exp(-4.179/T_9) \text{ sec}^{-1}$$

(0.520 MeV resonance)

$$\frac{1}{\tau_{^4\text{He}}(^9\text{Be})} = \frac{1}{1.39 \times 10^{-5}} X_{^4\text{He}} \rho T_9^{-3/2} \exp(-4.822/T_9) \text{ sec}^{-1}$$

(0.600 MeV resonance).

These times are in the nanosecond range for $T_9 \geq 1$ and $\rho \sim 10^5$ gm-cm^{-3}.

Using the table we may construct the various expressions for the reaction $^{13}C(\alpha,n)^{16}O$. For the non-resonant case we have

$$[01] = 6.769 \times 10^{15}(1 + 0.013T_9^{1/3} + 2.04T_9^{2/3} + 0.184T_9) \times \rho T_9^{-2/3}\exp(-32.329T_9^{-1/3}) \text{ sec}^{-1}$$

$$\frac{1}{\tau_{^4He}(^{13}C)} = \frac{1}{5.913 \times 10^{-16}}(1 + 0.013T_9^{1/3} + 2.04T_9^{2/3} + 0.184T_9) \times X_{^4He}\rho T_9^{-2/3}\exp(-32.329T_9^{-1/3}) \text{ sec}^{-1} \quad (6)$$

$$\varepsilon_{^{13}C^4He} = 2.779 \times 10^{32}(1 + 0.013T_9^{1/3} + 2.04T_9^{2/3} + 0.184T_9) \times X_{^4He}X_{^{13}C}\rho T_9^{-2/3}\exp(-32.329T_9^{-1/3}) \text{ erg-gm}^{-1}\text{-sec}^{-1} .$$

The quantity $\log_{10}[\rho X_{^4He}\tau_{^4He}(^{13}C)]$ has been plotted in fig. 28, as a function of T_9, with the lifetime in years. As expected, the lifetime is a very sensitive function of temperature, especially for $T_9 < 0.2$. See Table 3.

The rate of the $^{13}C(\alpha,n)^{16}O$ reaction in stars has been discussed by several authors (Cameron 1955, Burbidge 1957, Caughlan and Fowler 1964, and Reeves 1966). There are two

temperature regions in which it plays a part in neutron production. While hydrogen is burning via the CNO-cycle, an equilibrium concentration of ^{13}C exists. Just before the onset of helium burning, at a temperature around $T_9 = 0.08$, the possibility exists that the $^{13}C(\alpha, n)^{16}O$ reaction could produce neutrons. However, the conditions prevailing in the core of the star are such that very few neutrons are made available for capture by the heavier elements. This is because of the low abundance of ^{13}C nuclei ($\sim$ 1% of all CNO nuclei), and because of the presence of ^{14}N ($\sim$ 95% of CNO nuclei). Many neutrons are absorbed by the reaction $^{14}N(n, p)^{14}C$. Regeneration of the neutrons by $^{12}C(p, \gamma)^{13}N \rightarrow {}^{13}C(\alpha, n)^{16}O$ is not sufficiently rapid to act as an antidote to the ^{14}N. If we assume the number of iron group "seed" nuclei to be 1/70 of the number of CNO nuclei, then less than 1 neutron is available for capture by each heavy metal nucleus. For these reasons, the reaction $^{13}C(\alpha, n)^{16}O$ only supplies neutrons for capture on a very long time scale during the hydrogen-burning phase.

However, the situation changes after the hydrogen in the center of the star has been converted to helium, and the helium core heats up sufficiently to begin burning via the $3\,^4He \rightarrow {}^{12}C$ process. The star has now reached the giant stage, and its core temperature is in the vicinity of $T_9 = 0.1$. It is now possible for a small number of protons from the inner edge of the hydrogen envelope to be introduced into the core, where they are immediately captured by ^{12}C nuclei and thus form ^{13}C. Since there are only a limited number of protons available in this region, the reaction $^{13}C(p, \gamma)^{14}N$ is inhibited. Instead, the $^{13}C(\alpha, n)^{16}O$ reaction now takes place unimpeded, supplying a large number of neutrons which are captured by the heavy elements.

Equation (6) of this section may be used to compute the ^{13}C lifetime under the two conditions specified above. For the first case, at the termination of the CNO-cycle in the core, take $T_9 = 0.08$, and $\rho \sim 10^4$ gm-cm^{-3}. Since most of the hydrogen in the core has been consumed, $X_{^4He} \simeq 1$. The lifetime obtained is $\sim 10^5$ yr, demonstrating that the neutrons are indeed produced on a slow time scale.

Secondly, allow protons to be mixed into the helium-burning core at $T_9 = 0.1$, and assume a density of $\sim 5 \times 10^4$ gm-cm^{-3}. A lifetime of ~ 100 yr results. It is important to note that these temperatures and densities are only rough estimates. In fact, the density is changing very rapidly near the core boundary, and since the lifetime is such a sensitive function of temperature, a wide range of equilibrium situations will prevail wherever the ^{13}C is burning. However, it is clear that under these conditions the neutrons will be produced on a rapid time scale, permitting the formation of the heavier elements, i.e. those with $A \geq 100$. It appears that above a temperature of $T_9 \sim 0.25$, the $^{13}C(\alpha, n)^{16}O$ reaction will no longer be an important neutron source in the dense helium core, because the rate of formation of ^{13}C is limited by the 10-min β-decay of ^{13}N. Other reactions without this limitation, like $^{21}Ne(\alpha, n)^{24}Mg$, will become prevalent at the higher temperatures.

APPENDIX I Stilbene Response to Protons

Treating only single neutron-proton interactions in the stilbene crystal, the energy distribution of recoil protons from a monoenergetic neutron beam can be obtained in a straightforward manner. If the neutron energy is below 14 MeV, the elastic scattering in the center-of-mass system is isotropic. From this fact it is easily shown that the number of recoil protons is independent of proton energy, up to the maximum energy available to them. This energy is simply the neutron energy. In other words,

$$\frac{dN_p}{dE_p} = \begin{cases} \text{constant for } 0 < E_p \leq E_n \\ 0 \text{ for all other } E_p \end{cases}$$

The observed pulse-height spectrum differs from the theoretical rectangular shape for several reasons. It turns out that the luminous output of the stilbene is not proportional to the energy that the proton leaves in the crystal. A semi-empirical formula due to Birks (1953) allows us to write

$$\frac{dP}{dE_p} = \frac{1}{1 + kB\frac{dE}{dx}}$$

where P is the pulse height, and kB is a constant. For electrons of reasonable energy, dE/dx is very small, and can be neglected. This produces a direct proportionality between pulse height and

energy loss. For protons in the MeV region, dE/dx cannot be neglected, and the pulse height is not a linear function of the energy loss. In various measurements made by the author, the observed pulse height dependence on proton energy could be closely fit by a function of the form $P = A(E_p)^m$, where A is a constant of normalization, and m is a number in the vicinity of 1.4.

The effect of the non-linear response of stilbene is to compress the pulse-height spectrum at lower energies. This is illustrated by fig. 20, which shows the pulse-height spectrum on a semi-logarithmic scale obtained from the two reactions $^9Be(\alpha, n_0)^{12}C$ and $^9Be(\alpha, n_1)^{12}C^*(4.43)$. The higher energy group has an energy of 6.24 MeV and the lower energy group has an energy of 1.88 MeV.

A second factor which causes distortion of the pulse-height spectrum is statistical fluctuations. These occur in both the number of photons produced by the decaying lattice molecules, and in the number of photoelectrons emitted at the photocathode. As a result of these fluctuations, the pulse-height spectrum no longer has a sharp upper limit, but instead is folded with a gaussian. The width of this gaussian is usually several tenths of an MeV. It is common practice to assign the point at which the "rectangular" distribution drops to one-half its value as the energy corresponding to the maximum proton energy.

For the reasons stated above, the energy resolution of a stilbene crystal used as a fast neutron detector is quite poor. For precise determinations of neutron energies, other methods such as time-of-flight and (n, p) and (n, α) reactions in silicon detectors

are far superior. The advantage of stilbene lies in its high efficiency and its ability to discriminate against gamma rays (see Appendix II).

In all the efficiency calculations done in this thesis, effects such as (a) loss of protons from the end of the crystal, (b) loss of protons from the sides of the crystal, (c) scattering from carbon nuclei, and (d) double scattering from hydrogen, have all been neglected. It turns out that neglecting these factors usually causes only a small error. The reasons for this are: (1) some of the effects actually work to cancel one another, i. e. (a) and (c) with (d), and (2) the total integrated number of counts does not change. Counts may be shifted from lower to higher energies and vice-versa. Since the quantities determined from these experiments involved adding up the total number of counts between widely spaced limits, the effects of the above-mentioned secondary or geometrical factors are minimized, and are therefore neglected here.

APPENDIX II Pulse-Shape Discrimination

Within the last decade a new technique for detecting fast neutrons has evolved, based on a phenomenon peculiar to certain organic scintillators. It is found that the decay times of the scintillations from these materials increases with the specific ionization of the detected particle (Wright 1956). Actually, it has been shown that the decay consists of a slow and a fast component, and it is the relative amounts of each which is determined by the nature of the ionizing particle. Thus the scintillations due to protons (caused by recoil from a neutron) and to electrons (produced when an incident gamma ray undergoes Compton scattering or pair production) may be separated electronically using their different scintillation pulse shapes (Owen 1958).

Some scintillators which are useful for pulse-shape discrimination are stilbene, quaterphenyl, and anthracene. These are solid crystals. Certain liquid scintillators exhibit the same decay-time characteristics, provided that all dissolved oxygen is first removed (Brooks 1959).

Circuit Details

The circuit chosen was one devised by Daehnick and Sherr (Daehnick 1961) (see upper left corner of fig. 12). The operation of the pulse-shape discriminator is as follows. The current pulse through the photomultiplier may be approximated by the sum of two components:

$$I(E,t) = I_0(E)[\exp(-t/\tau_f) + a(E)\exp(-t/\tau_s)]$$

where τ_f is a fast decay time, $\leq$ 10 ns, and τ_s is a slow decay time, usually several hundred ns. The coefficient a(E) depends on dE/dx of the charged particle which is actually detected. For electrons, a(E) is small (about 0.011 for several MeV), and increases for more heavily ionizing particles (about 0.021 for protons of similar energy) (Daehnick 1961). It is the excess of slow component possessed by proton pulses which enables them to be separated from electron pulses.

The photomultiplier current pulse is integrated by stray capacities at the anode and at the second-last dynode. The anode capacity is discharged through a low resistance R_1 = 3.9 kΩ (integrating time ~ 10 ns), whereas the dynode capacity sees a 1 MΩ resistance R_2 (integrating time several μs). As a consequence, the voltage pulse obtained from the anode consists of only a sharp negative spike. The dynode pulse is a positive pulse which contains a slowly decaying tail. Both pulses are stretched by means of diodes CR1 and CR2, and added together on a common load resistor R_3. Time constants controlled by capacitors R, C, and F are adjusted so that electrons produce a zero or negative output, while protons produce a positive output pulse. This is the PSD pulse referred to in the main body of the text.

An additional feature of this circuit is the coupling network between the fast (anode) channel and the slow (dynode) channel. This network consists of trimming capacitor C, diode CR3, and resistor R_4. It acts to effectively short-circuit the slow channel to ground for the first few hundred ns after the arrival of a pulse. In this way the

pulse derived from the slow channel is proportional only to the amount of slow decay component.

REFERENCES

Amaldi, E. 1959, Handbuch der Physik (Flügge) Vol. XXXVIII/2, 115.

Bennet, W. E., Roys, P. A., and Toppel, B. J. 1954, Phys. Rev. 93, A924.

Birks, J. B. 1953, "Scintillation Counters", 93.

Brooks, F. D. 1959, Nucl. Instr. and Meth. 4, 151.

Burbidge, E. M., Burbidge, G. R., Fowler, W. A., and Hoyle, F. 1957, Rev. Mod. Phys. 29, 547.

Cameron, A. G. W. 1954, Phys. Rev. 93, 932
1955, Ap. J. 121, 144.

Caughlan, G. R., and Fowler, W. A. 1964, Ap. J. 139, 1180.

Chadwick, J. 1932, Proc. Royal Soc. London A136, 692.

Daehnick, W., and Sherr, R. 1961, Rev. Sci. Instr. 32, 666.

Fowler, W. A., Caughlan, G. R., and Zimmerman, B. A. 1967, Annual Review of Astronomy and Astrophysics (to be published).

Garwin, R. L., Hutchinson, D., Penman, S., and Shapiro, G. 1959, Rev. Sci. Instr. 30, 105.

Greenstein, J. L. 1954, "Modern Physics for the Engineer", First Series, 267.

Hughes, D. J. 1958, "Neutron Cross-Sections", 2nd Ed., 74, 97.

James, D. B., Jones, G. A., and Wilkinson, D. H. 1956, Phil. Mag. 1, 949.

Jones, G. A., and Wilkinson, D. H. 1951, Proc. Phys. Soc. A64, 756.
1953, Proc. Phys. Soc. A66, 1176.

Marion, J. B. 1961, Rev. Mod. Phys. 33, 139.

Owen, R. B. 1958, IRE Trans. in Nucl. Sci. NS-5, 198.

Pearson, J. D. 1963, Thesis, California Institute of Technology.

Porat, D. I., and Ramavataram, K. 1961, Proc. Phys. Soc. 78, 1135.

Reeves, H. 1966, Ap. J. 146, 447.

Rusbridge, M. G. 1956, Proc. Phys. Soc. A69, 830.

Vogl, J. L. 1963, Thesis, California Institute of Technology.

Walton, R. B., Clement, J. D., and Boreli, F. 1954, Phys. Rev. 107, 1065.

Wenzel, W. A. 1952, Thesis, California Institute of Technology.

Whaling, W. 1958, Handbuch der Physik (Flügge) Vol. XXXIV, 13.

Wright, G. T. 1956, Proc. Phys. Soc. B69, 358.

TABLE 1

Quantities used in computing the yield of the $^{13}C(\alpha, n)^{16}O$ reaction, discussed in Section (g) (1), part II, and Section (a) part V.

E_B (MeV)	I_1 (10^{-22})	I_2 (10^{-22})	$\frac{n}{200}$	Y_{exp}	Y_{calc}	$\sigma(E_L)$ (nb)
.475	1.15	.519	18	88	83.1	2.93
.500	2.81	1.33	21	245	241.5	6.83
.525	6.43	3.19	8	238	215.1	14.9
.550	13.9	7.23	4	225	237.8	31.0
.575	28.7	15.6	3	384	375.2	61.2
.600	56.6	32.0	2	492	503.2	116.
.625	107.	63.1	4	1884	1945.9	211.
.650	196.	120.	.5	474	453.6	371.
.675	348.	221.	.5	826	819.0	632.
.700	599.	393.	.25	744	717.9	1047.

TABLE 2

Coefficients of Legendre polynomials required to fit angular distributions from the reactions $^{9}Be(\alpha, n_0)^{12}C$ and $^{9}Be(\alpha, n_1)^{12}C^*$ (4.43). All are normalized such that the coefficient of $P_0(\cos\theta) = 1$.

$^{9}Be(\alpha, n_0)^{12}C$

E_B	A_0	A_1	A_2	A_3	A_4
.480	1	$-.09 \pm .03$	$-.09 \pm .04$	$+.35 \pm .05$	---
.520	1	$-.05 \pm .02$	$-.09 \pm .02$	---	---
.593	1	$-.41 \pm .02$	$+.01 \pm .03$	$-.56 \pm .04$	$+.19 \pm .03$
.608	1	$-.41 \pm .02$	$-.01 \pm .03$	$-.40 \pm .04$	$+.26 \pm .03$

$^{9}Be(\alpha, n_1)^{12}C^*(4.43)$

E_B	A_0	A_1	A_2	A_3	A_4
.480	1	$-.09 \pm .02$	---	---	---
.520	1	$-.21 \pm .02$	$+.08 \pm .02$	---	---
.593	1	$-.24 \pm .01$	---	---	---
.608	1	$-.04 \pm .02$	$-.06 \pm .02$	$-.06 \pm .02$	---

TABLE 3

Lifetime of the ^{13}C nucleus to interaction with ^{4}He via the reaction $^{13}C(\alpha,n)^{16}O$. The lifetime is given in years, and the density is given in gm-cm^{-3}. See page 45.

T_9	$\log_{10}[\rho X_{^4He} \tau_{^4He}(^{13}C)]$
.02	+27.80
.04	+17.30
.06	+12.20
.08	+8.98
.10	+6.69
.12	+4.94
.14	+3.54
.16	+2.39
.18	+1.42
.20	+0.57
.25	-1.11
.30	-2.40
.40	-4.28
.50	-5.62

Fig. 1

Schematic diagram of the regulating system for the magnetic analyser, 700 kV accelerator. Individual circuits are given for the transistor panel (fig. 2), the coarse regulator (fig. 3), and the DC amplifier and driver (fig. 4). See page 6.

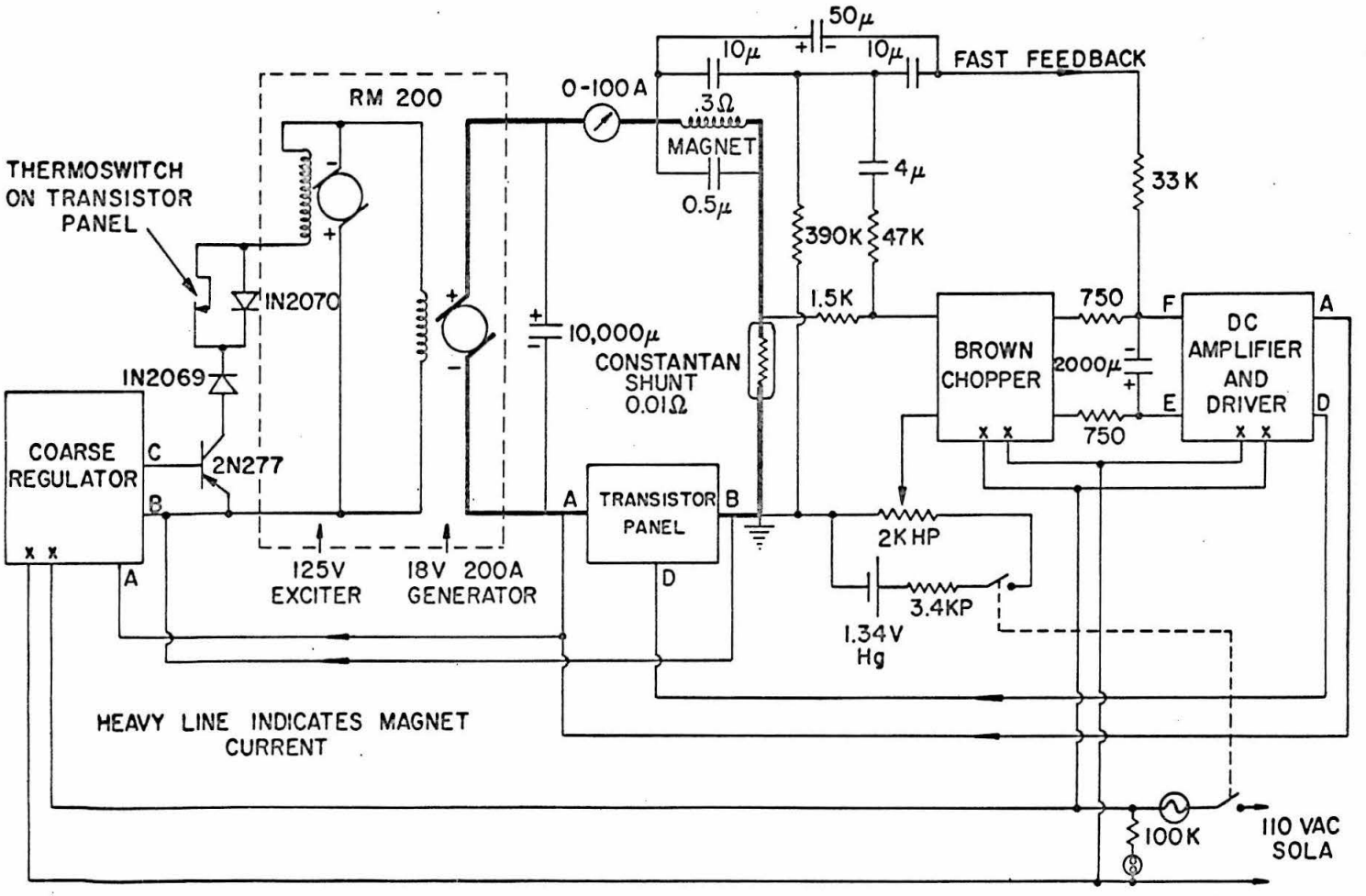
MAGNETIC ANALYSER CURRENT SUPPLY AND REGULATOR
50μ
10μ
10μ
FAST FEEDBACK
0-100A
.3Ω
MAGNET
0.5μ
4μ
33K
390K
47K
RM 200
THERMOSWITCH ON TRANSISTOR PANEL
IN2070
IN2069
1.5K
750
F
A
10,000μ
CONSTANTAN SHUNT 0.01Ω
BROWN CHOPPER
2000μ
DC AMPLIFIER AND DRIVER
E
D
750
COARSE REGULATOR
C
2N277
B
A
TRANSISTOR PANEL
B
2K HP
3.4KP
1.34V Hg
D
125V EXCITER
18V 200A GENERATOR
HEAVY LINE INDICATES MAGNET CURRENT
100K
110 VAC SOLA

Figure 1

Fig. 2

The pass transistors and the driver transistor for the magnetic analyser regulating system. These transistors are mounted on a water-cooled copper heat sink. See fig. 1 for complete circuit details, and also page 6.

TRANSISTOR PANEL

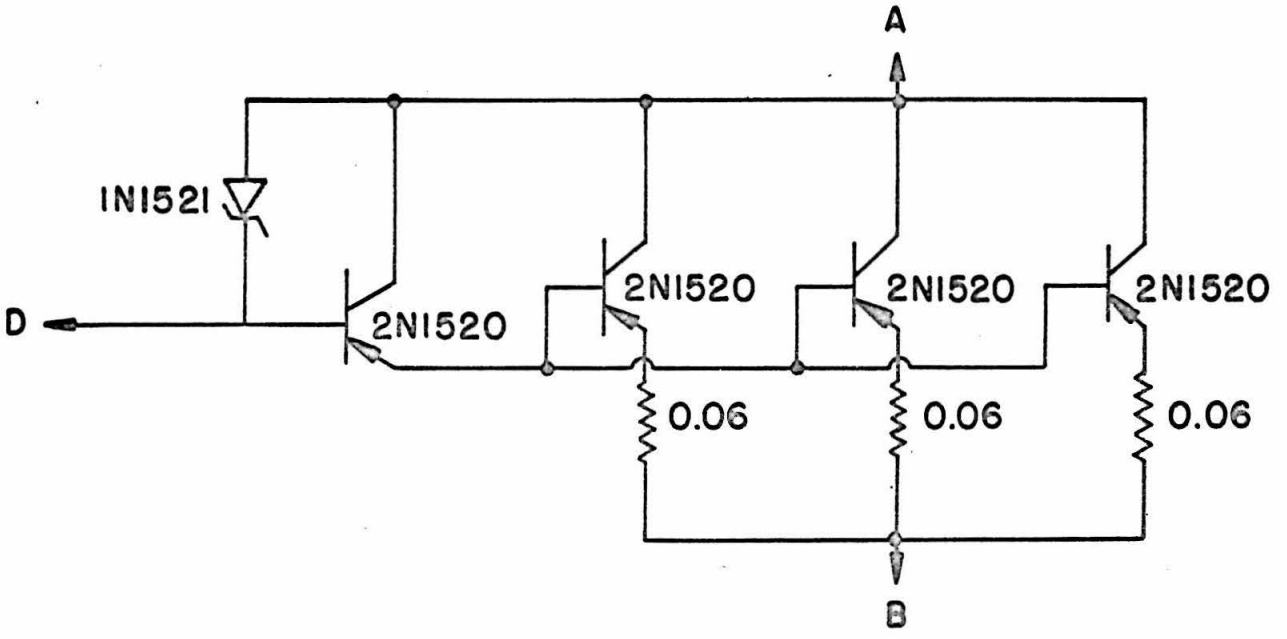

MOUNTED ON WATER-COOLED HEAT SINK

Figure 2

Fig. 3

Coarse regulator for field winding of DC generator, magnetic analyser regulator system. The voltage across the transistor panel, fig. 2, appears between points A and B. This is compared with the voltage at the emitter of the 2N388 transistor, which is set in the vicinity of 1-2 volts by the 2N525 transistor. The output is taken from points C and B to the base of the 2N277 transistor, fig. 1. Current in this transistor passes through the field windings. If the voltage across the transistor panel rises above 2 volts, the coarse regulator decreases the generator field current, and thus its output voltage. See page 6.

COARSE REGULATOR

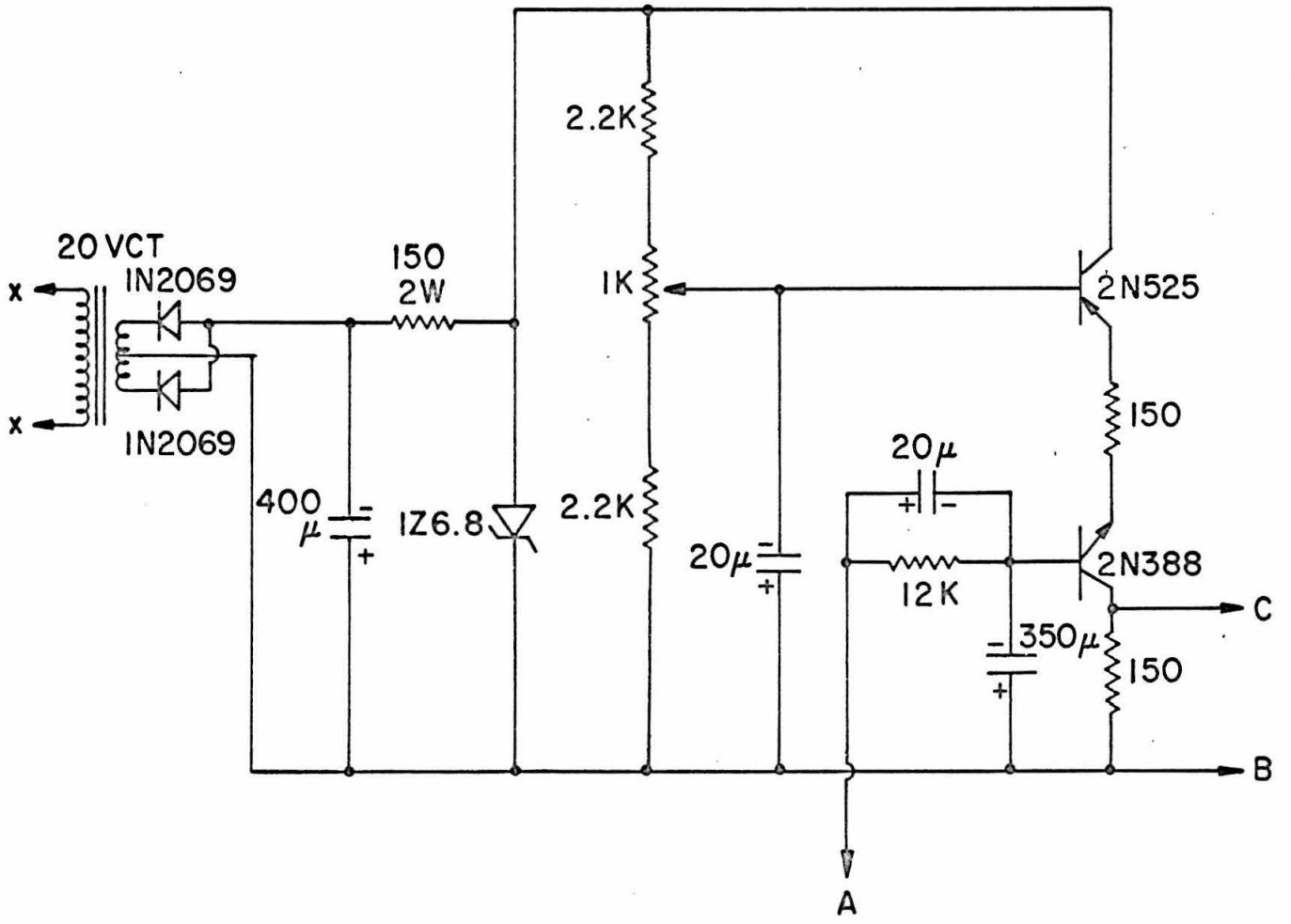

Figure 3

Fig. 4

DC amplifier and driver, magnetic analyser regulator for 700 kV accelerator. This circuit amplifies the DC error signal received from the chopper amplifier and raises it to a level sufficient to drive the transistors of the transistor panel, fig. 2. See fig. 1 and page 6.

DC AMPLIFIER AND DRIVER

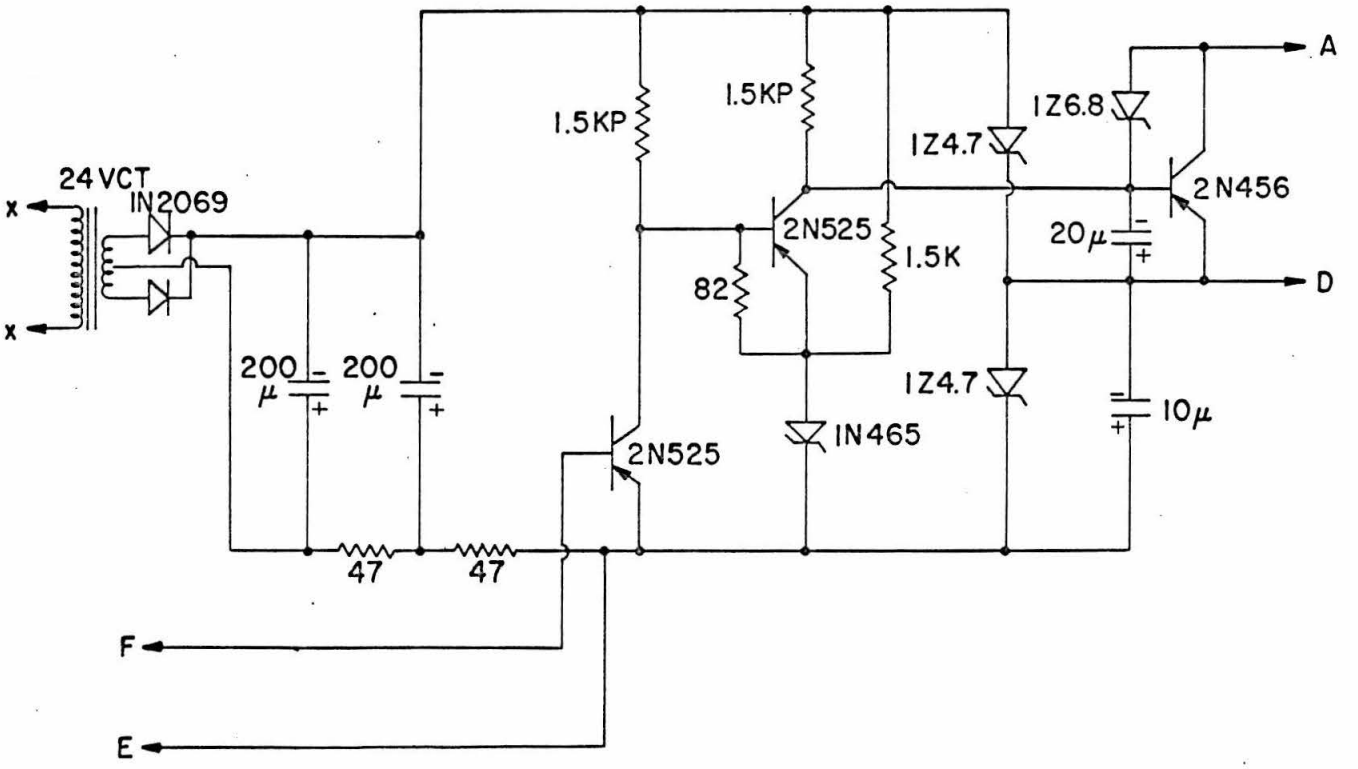

Figure 4

Fig. 5

Temperature controller for Hall probe. The thermistor R_T is one arm of an AC-excited bridge. Current pulses are supplied by the 2N1395-2N277 combination to the heater when the bridge is unbalanced. Equilibrium is reached at 42°C. See page 8.

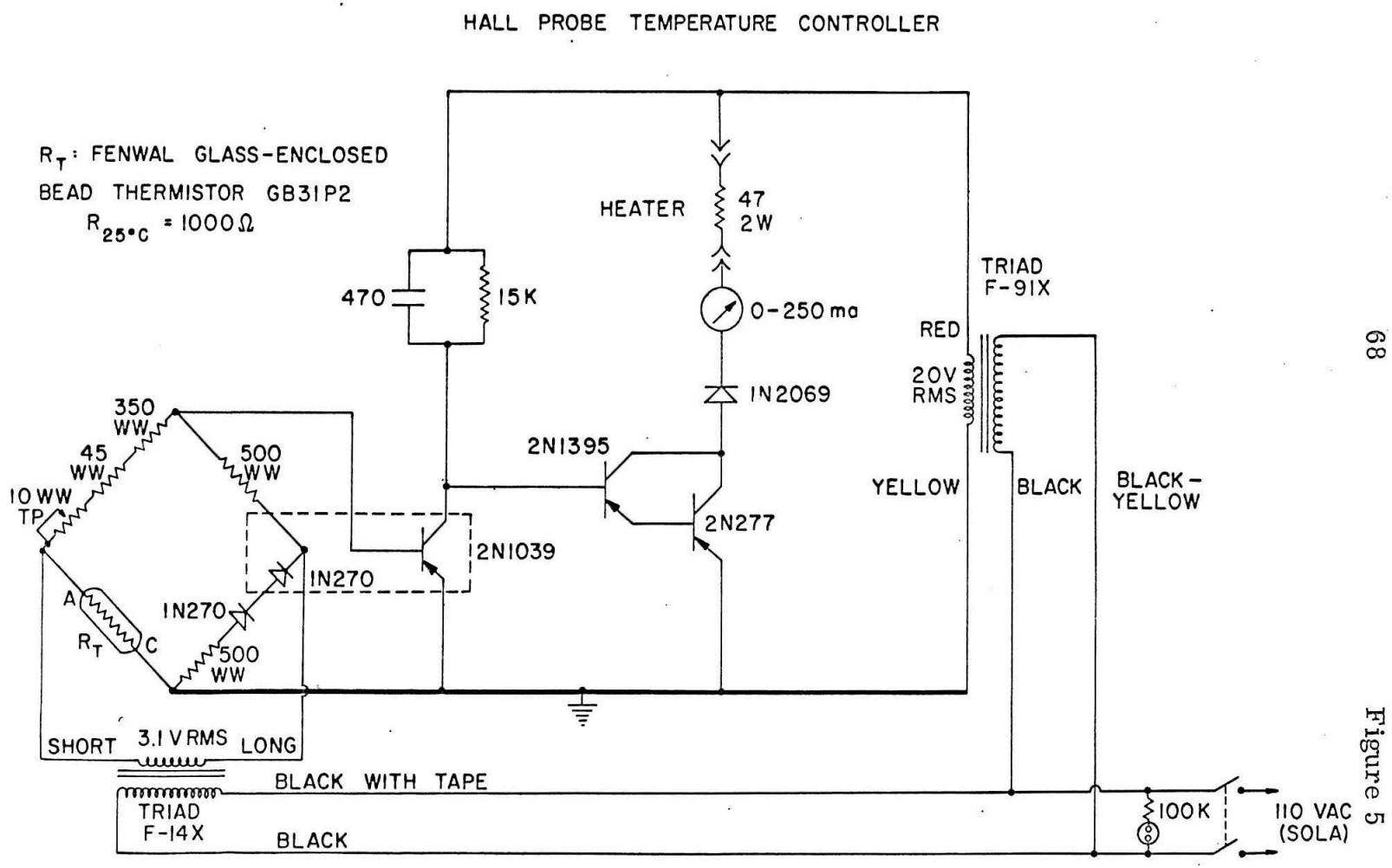
HALL PROBE TEMPERATURE CONTROLLER
R_T: FENWAL GLASS-ENCLOSED
BEAD THERMISTOR GB31P2
$R_{25°C}$ = 1000Ω
HEATER
47
2W
470
15K
0-250 ma
IN2069
TRIAD
F-91X
RED
20V
RMS
YELLOW
BLACK
BLACK-
YELLOW
350
WW
45
WW
10 WW
TP
500
WW
2N1395
2N277
2N1039
IN270
IN270
A
R_T
C
500
WW
SHORT
3.1 VRMS
LONG
BLACK WITH TAPE
TRIAD
F-14X
BLACK
100K
110 VAC
(SOLA)

Figure 5

Fig. 6

Current supply for Hall probe. Supplies 225 ma very highly regulated. See page 8.

HALL PROBE PRECISION CURRENT SUPPLY

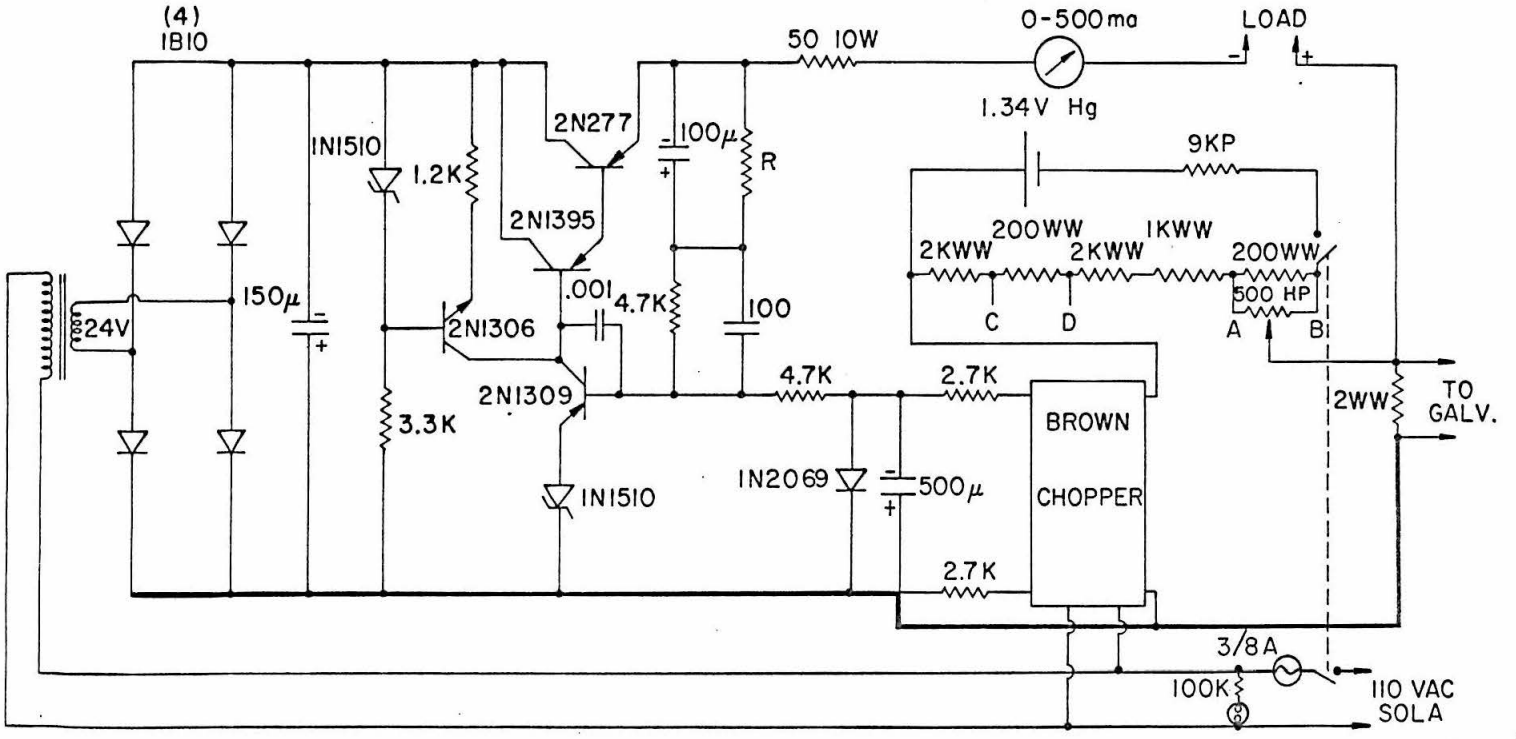

1) 225ma OPERATION: R = 470K

2) 100ma OPERATION: R = 68K
CONNECT A,B OF HELIPOT TO C,D

Figure 6

Fig. 7

Beam current indicator. The two field-effect transistors are connected in a voltmeter configuration. Since the entire circuit must be isolated from DC ground, it is built on an insulating circuit board, which is then mounted on a lucite panel. See page 12.

FIELD EFFECT TRANSISTOR BEAM CURRENT INDICATOR

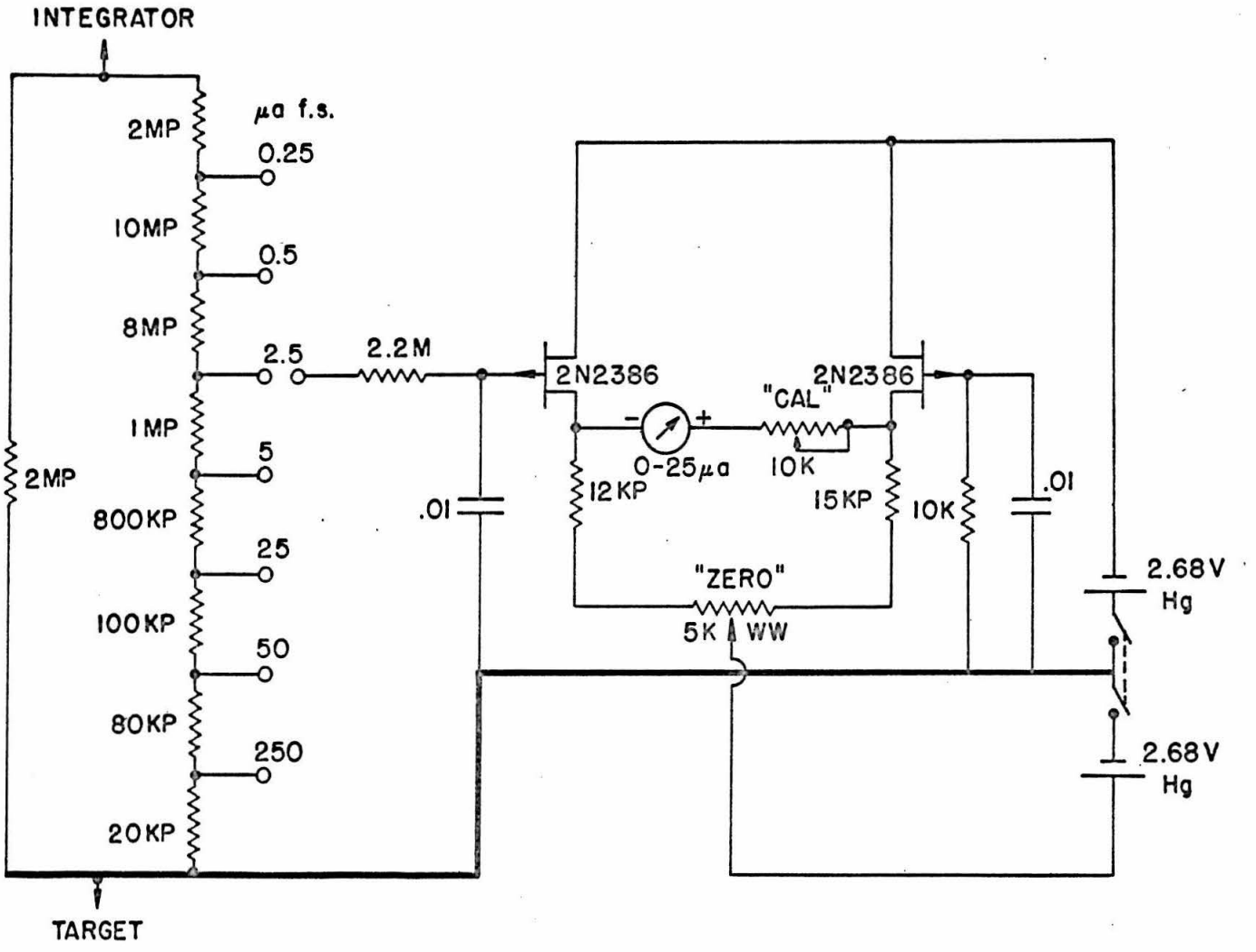

Figure 7

Fig. 8

Target holder used for the reaction $^{13}C(\alpha, n)^{16}O$. The target itself serves as the end vacuum seal. Also seen is one end of the cold sleeve surrounding the beam, which keeps carbon deposition during bombardment to a negligible rate. A viewing port is provided so that the beam spot can be observed during bombardment. See pages 12 and 13.

$^{13}C(\alpha,n)^{16}O$ TARGET HOLDER

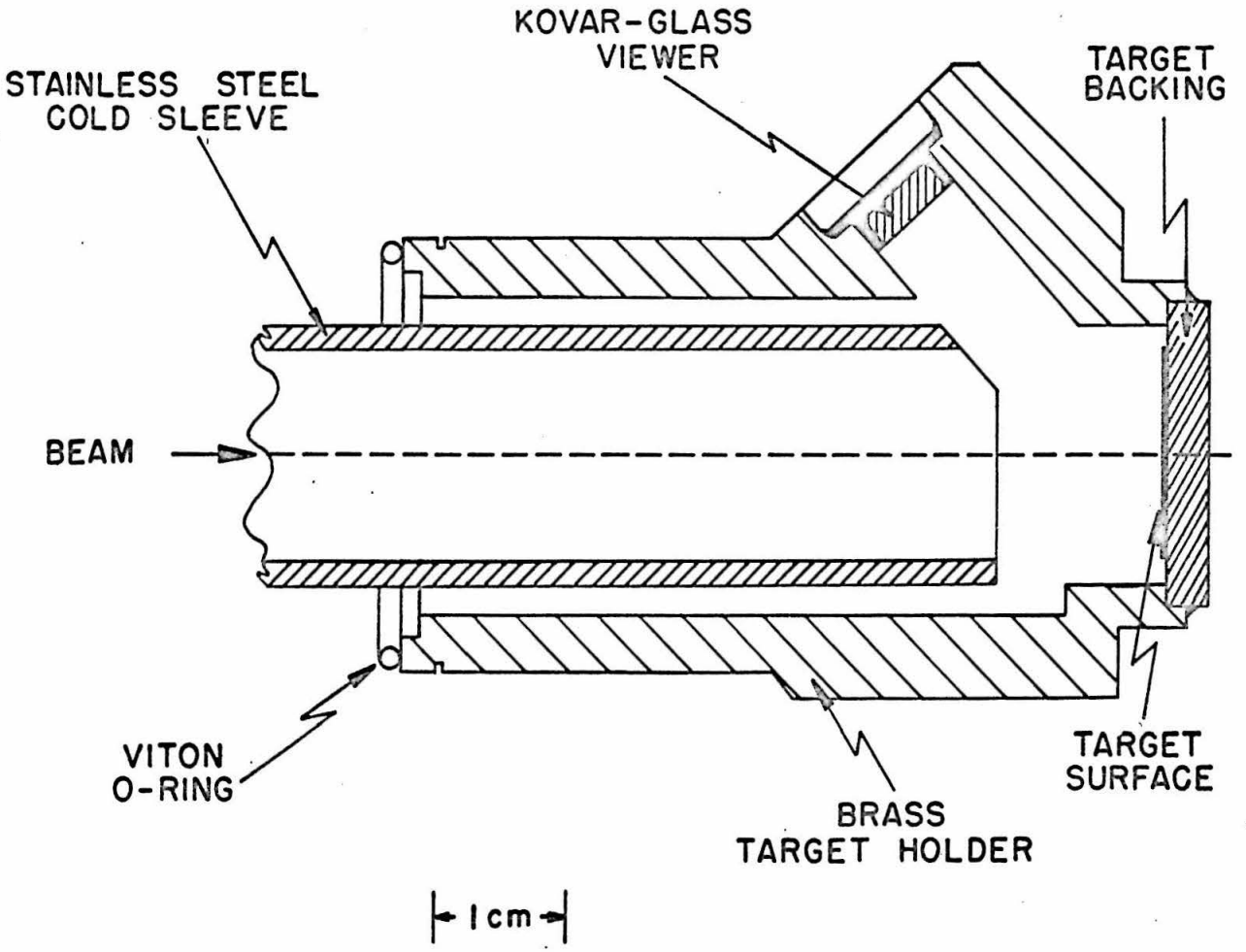

Figure 8

Fig. 9

Brass target chamber used for excitation function measurements on the reaction $^{9}Be(\alpha, n)^{12}C$. The large mass of copper used as the target support provided a heat sink which was cooled by an air blast. See page 12.

Figure 9

TARGET CHAMBER USED FOR $^{9}Be(\alpha,n)^{12}C$ EXCITATION FUNCTION MEASUREMENTS

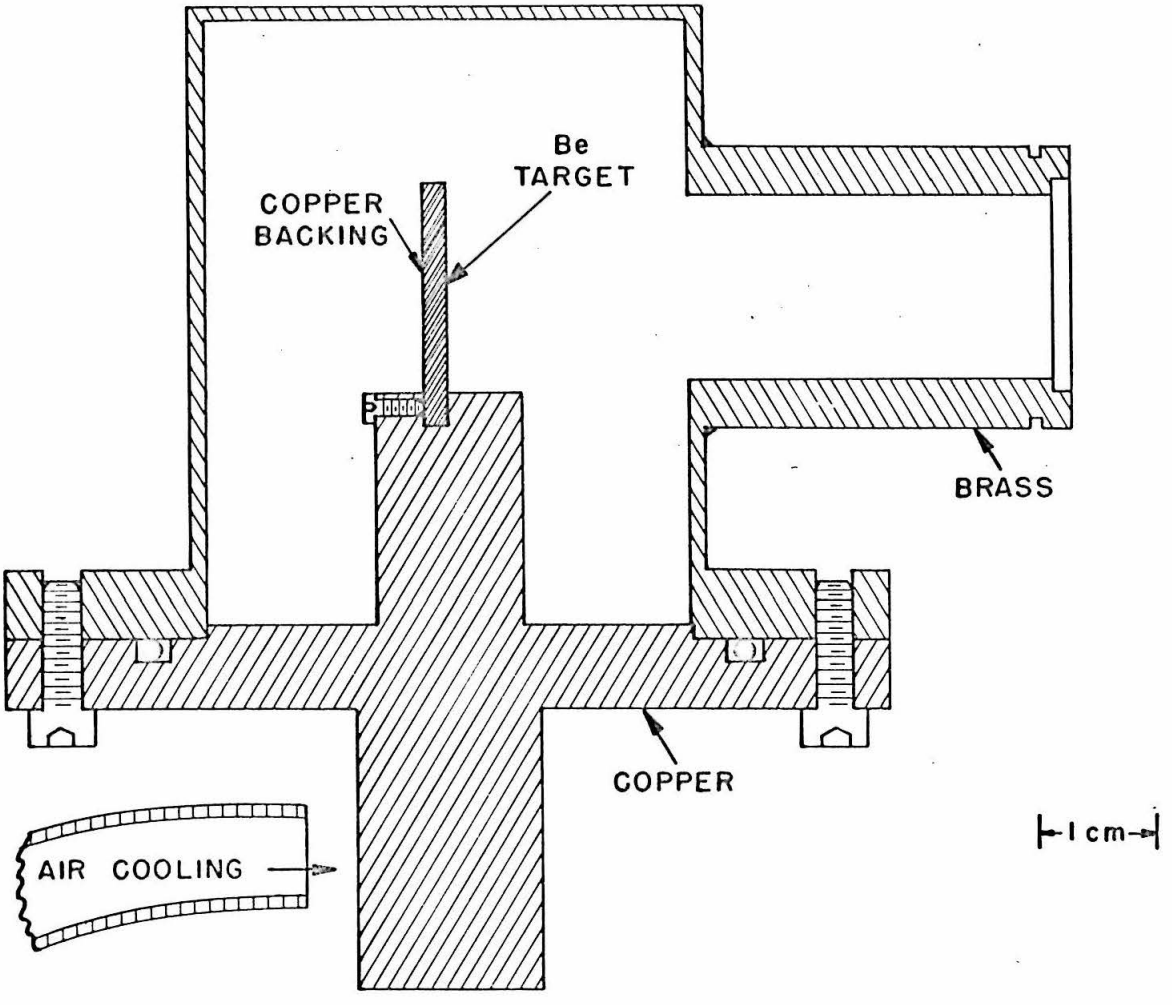

Fig. 10

Excitation function measurement on a thick ^{12}C and ^{13}C target of the reaction $^{13}C(p,\gamma)^{14}N$. The sharp resonance at 448.5 keV is seen as a steep step in the yield. See page 13 for details.

Figure 10

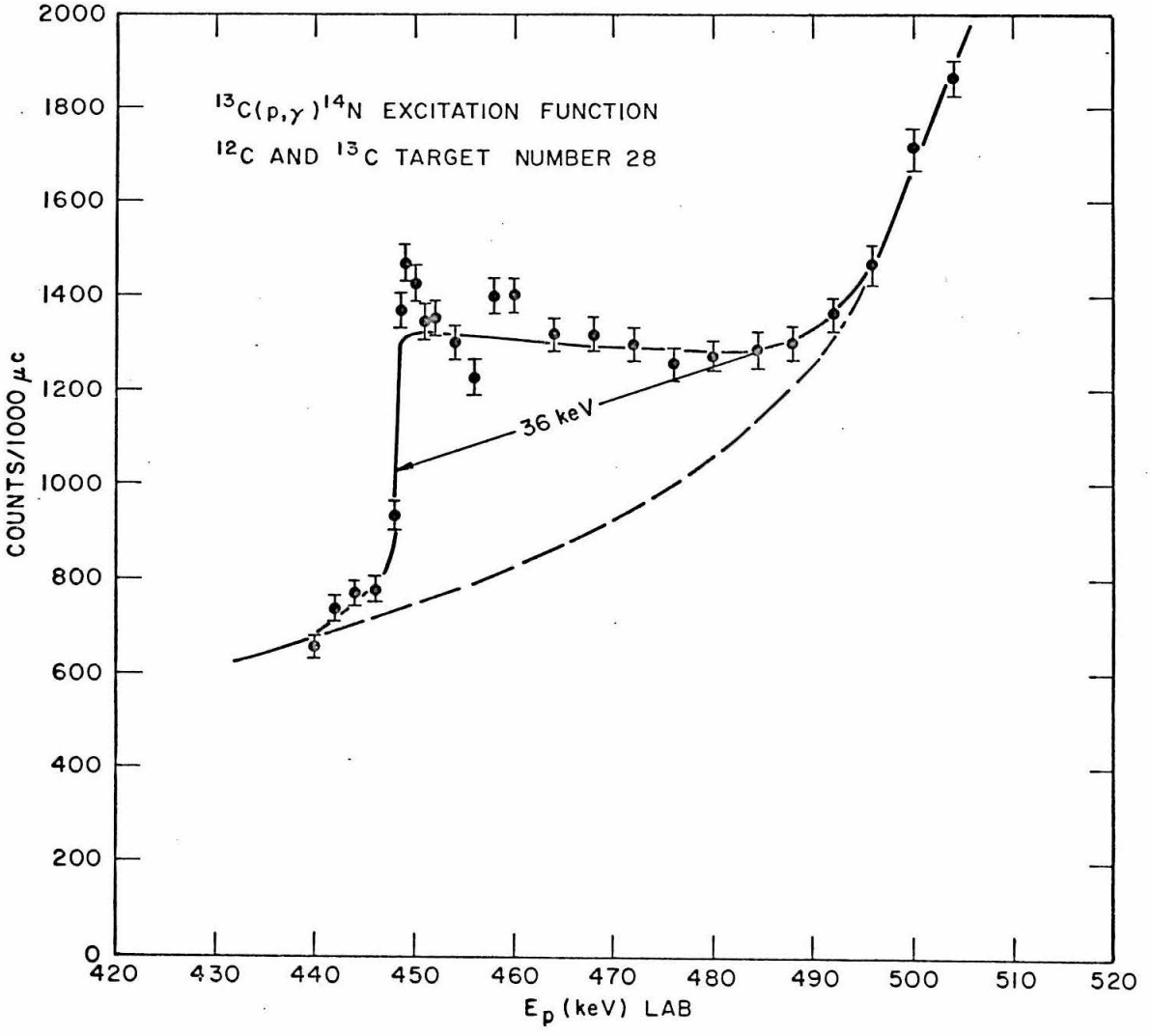
$^{13}C(p,\gamma)^{14}N$ EXCITATION FUNCTION
^{12}C AND ^{13}C TARGET NUMBER 28
36 keV
COUNTS/1000 μc
E_p (keV) LAB
0
200
400
600
800
1000
1200
1400
1600
1800
2000
420
430
440
450
460
470
480
490
500
510
520

Fig. 11

Block diagram of neutron counter electronics. The left-hand block is contained in the probe (fig. 12), and the schematic diagrams for the remaining blocks are found in figs. 13-15. See circuit description beginning page 15.

Figure 11

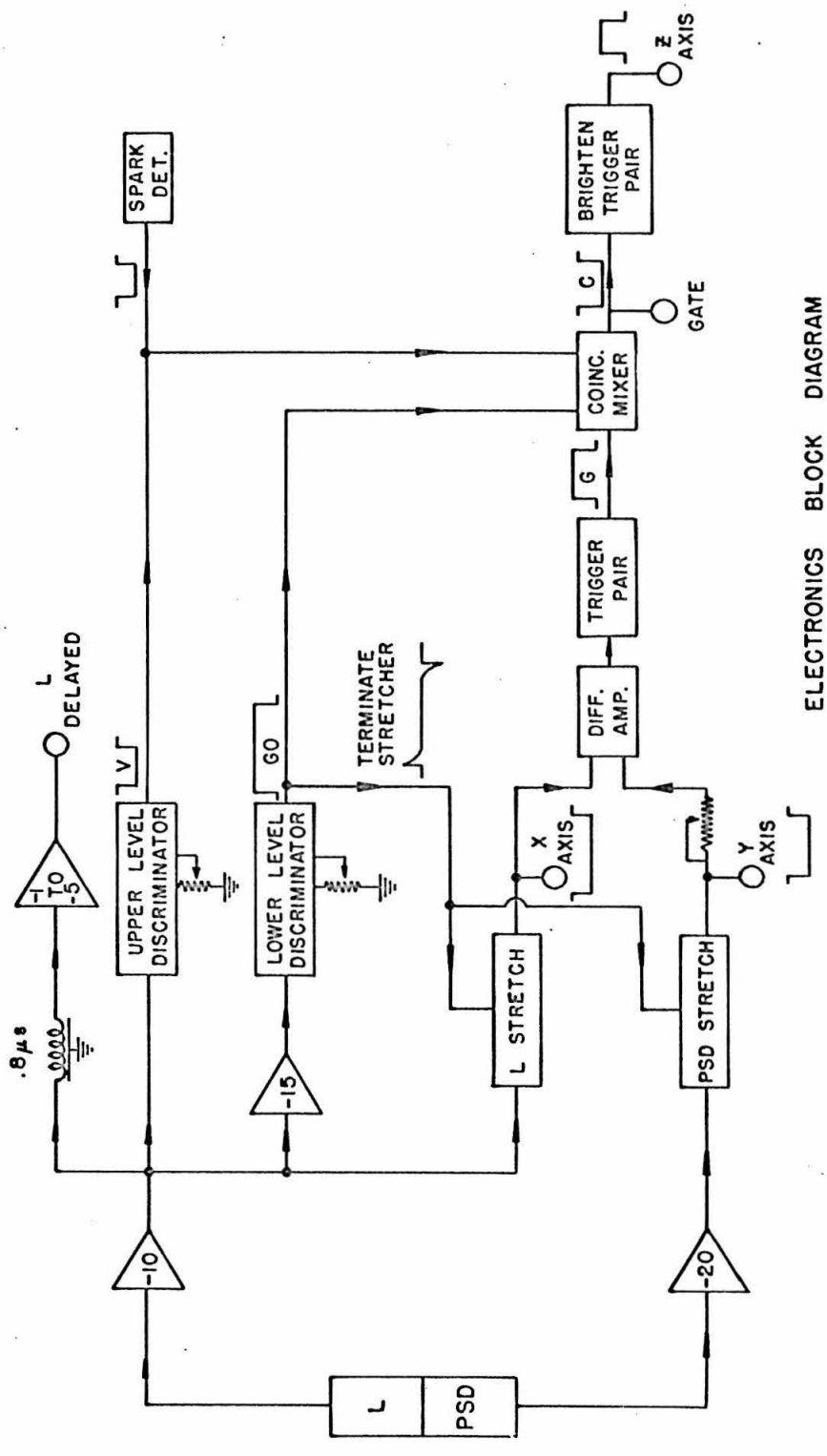
SPARK DET.
BRIGHTEN TRIGGER PAIR
Z AXIS
C
GATE
COINC. MIXER
G
TRIGGER PAIR
DIFF. AMP.
L DELAYED
V
GO
TERMINATE STRETCHER
-1 TO -5
UPPER LEVEL DISCRIMINATOR
LOWER LEVEL DISCRIMINATOR
.8 μs
-15
X AXIS
Y AXIS
L STRETCH
PSD STRETCH
-10
-20
L
PSD
ELECTRONICS BLOCK DIAGRAM

Fig. 12

Circuit diagram of pulse-shape discrimination probe, contained in the photomultiplier tube base. Included are the n-γ discrimination circuit, linear pulse preamplifier, and PSD pulse output circuit. Description of circuitry is given on pages 15 and 16.

PULSE-SHAPE DISCRIMINATOR PROBE

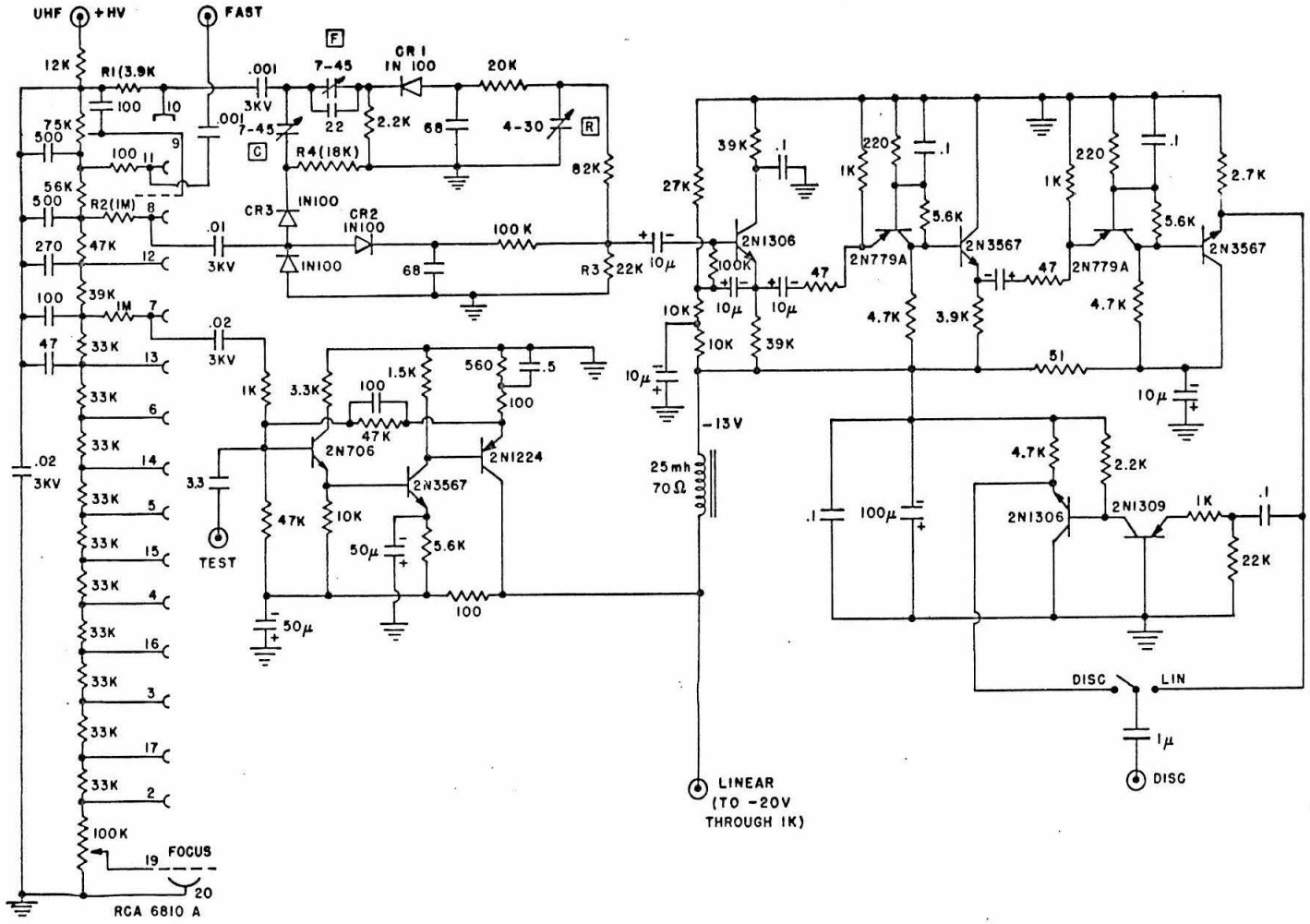

Figure 12

Fig. 13

Pulse-shape discrimination pulse analysis circuitry including linear pulse amplifier, lower level discriminator, linear pulse stretcher, delay line, and linear output amplifier. See block diagram (fig. 11) and description on page 16.

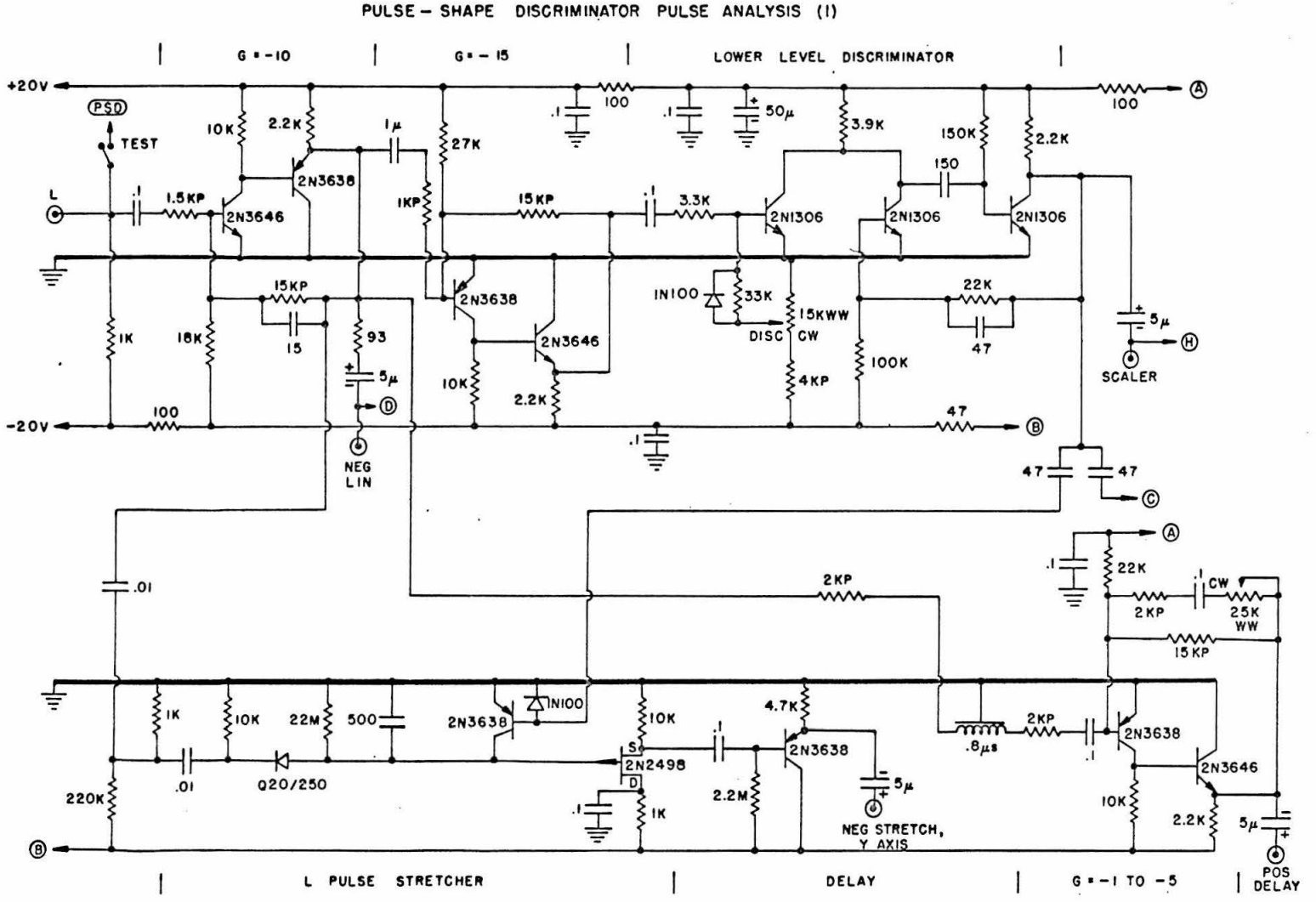
PULSE – SHAPE DISCRIMINATOR PULSE ANALYSIS (I)
G = -10
G = -15
LOWER LEVEL DISCRIMINATOR
+20V
-20V
PSD
TEST
L
10K
2.2K
1μ
27K
2N3638
2N3646
1.5KP
1KP
15KP
100
3.9K
150K
150
2.2K
3.3K
2N1306
IN100
33K
15KWW
DISC
CW
4KP
100K
22K
47
5μ
SCALER
1K
18K
15
93
NEG
LIN
47
.01
2KP
25K
WW
220K
500
22M
Q20/250
4.7K
2N2498
2.2M
NEG STRETCH,
Y AXIS
.8μs
L PULSE STRETCHER
DELAY
G = -1 TO -5
POS
DELAY

Figure 13

Fig. 14

Pulse-shape discriminator pulse analysis circuitry including PSD pulse amplifier, PSD stretcher, and linear pulse upper level discriminator. See block diagram (fig. 11) and description on page 16.

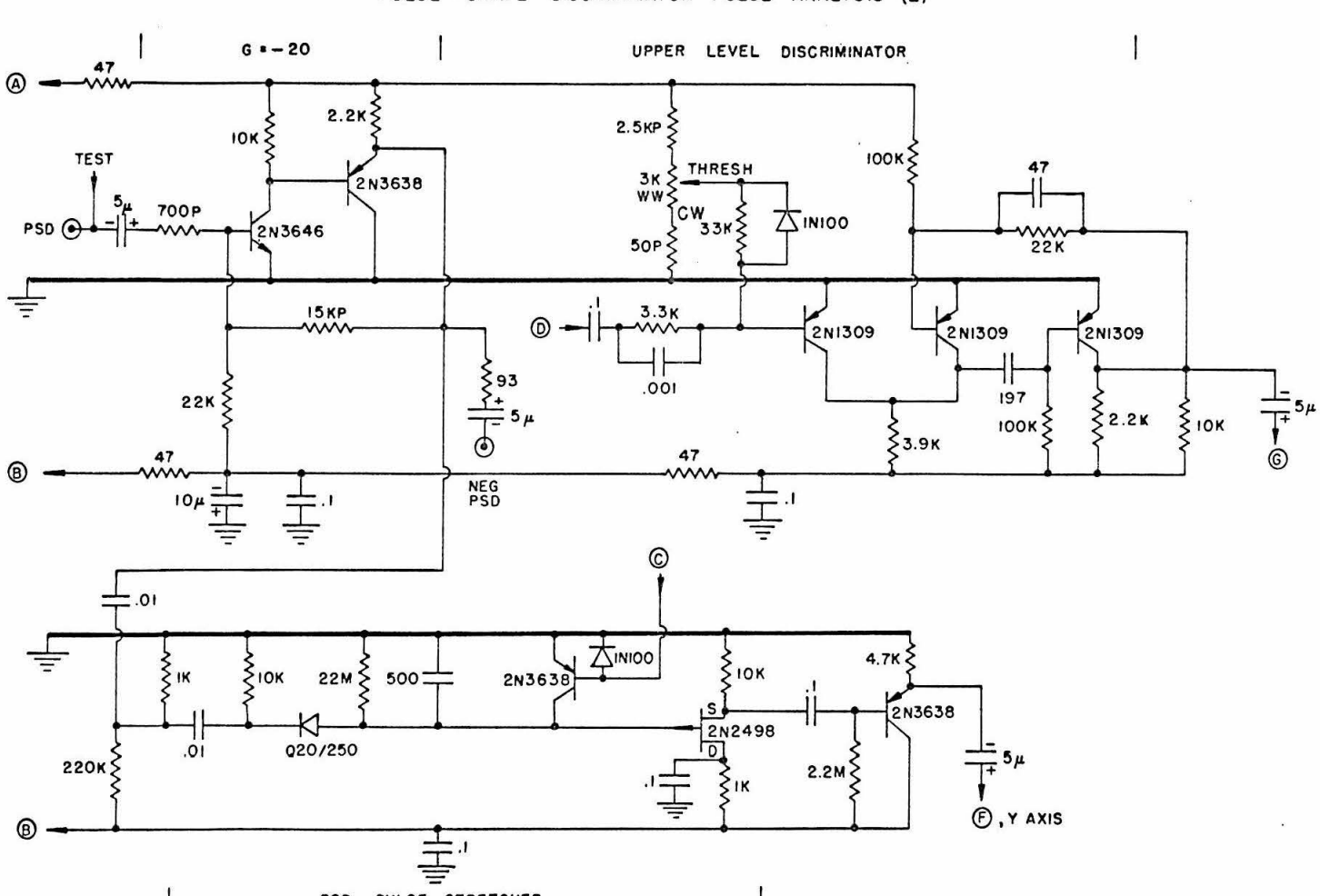
PULSE – SHAPE DISCRIMINATOR PULSE ANALYSIS (2)
G = – 20
UPPER LEVEL DISCRIMINATOR
47
2.2K
10K
2.5KP
100K
TEST
2N3638
3K
WW
THRESH
47
5μ
700P
PSD
2N3646
CW
33K
IN100
50P
22K
15KP
.1
3.3K
2N1309
2N1309
2N1309
93
5μ
.001
197
22K
100K
2.2K
10K
5μ
3.9K
47
47
10μ
.1
NEG
PSD
.1
.01
IK
10K
22M
500
2N3638
IN100
10K
4.7K
S
2N2498
D
.1
2N3638
220K
.01
Q20/250
.1
IK
2.2M
5μ
, Y AXIS
.1
PSD PULSE STRETCHER

Figure 14

Fig. 15

Pulse-shape discriminator pulse analysis including differential amplifier, trigger pair, coincidence mixer, brightener trigger pair, and scaler and gate output. See block diagram (fig. 11) and description on pages 16 and 17.

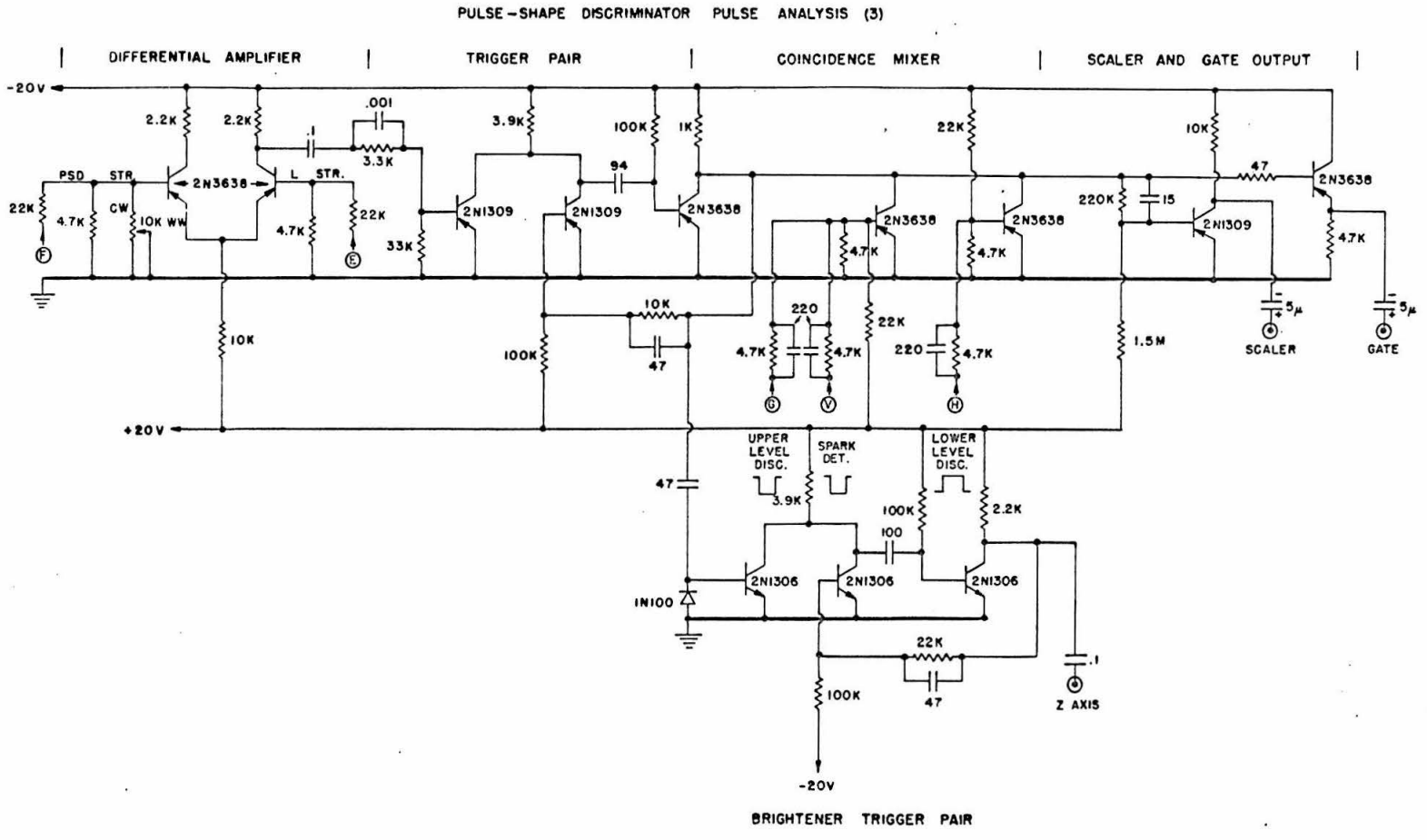
PULSE-SHAPE DISCRIMINATOR PULSE ANALYSIS (3)
DIFFERENTIAL AMPLIFIER
TRIGGER PAIR
COINCIDENCE MIXER
SCALER AND GATE OUTPUT
-20V
+20V
2.2K
2.2K
.001
.1
3.3K
3.9K
100K
1K
22K
10K
47
2N3638
PSD
STR
CW
10K WW
L
STR.
22K
4.7K
4.7K
33K
2N1309
2N1309
94
2N3638
2N3638
2N3638
4.7K
4.7K
220K
15
2N1309
4.7K
10K
100K
10K
47
220
4.7K
4.7K
22K
220
4.7K
1.5M
5μ
SCALER
5μ
GATE
F
E
G
V
H
UPPER LEVEL DISC.
SPARK DET.
LOWER LEVEL DISC.
47
3.9K
100K
100
2.2K
2N1306
2N1306
2N1306
IN100
22K
47
.1
Z AXIS
100K
-20V
BRIGHTENER TRIGGER PAIR

Figure 15

Fig. 16

Spark detector schematic. The input of this circuit is connected to the bleeder chain of the 700 kV accelerator, and it detects fast transients appearing there. The output is connected to the gate generator (upper circuit, fig. 17), which generates the "V" veto pulse. See page 18.

SPARK DETECTOR

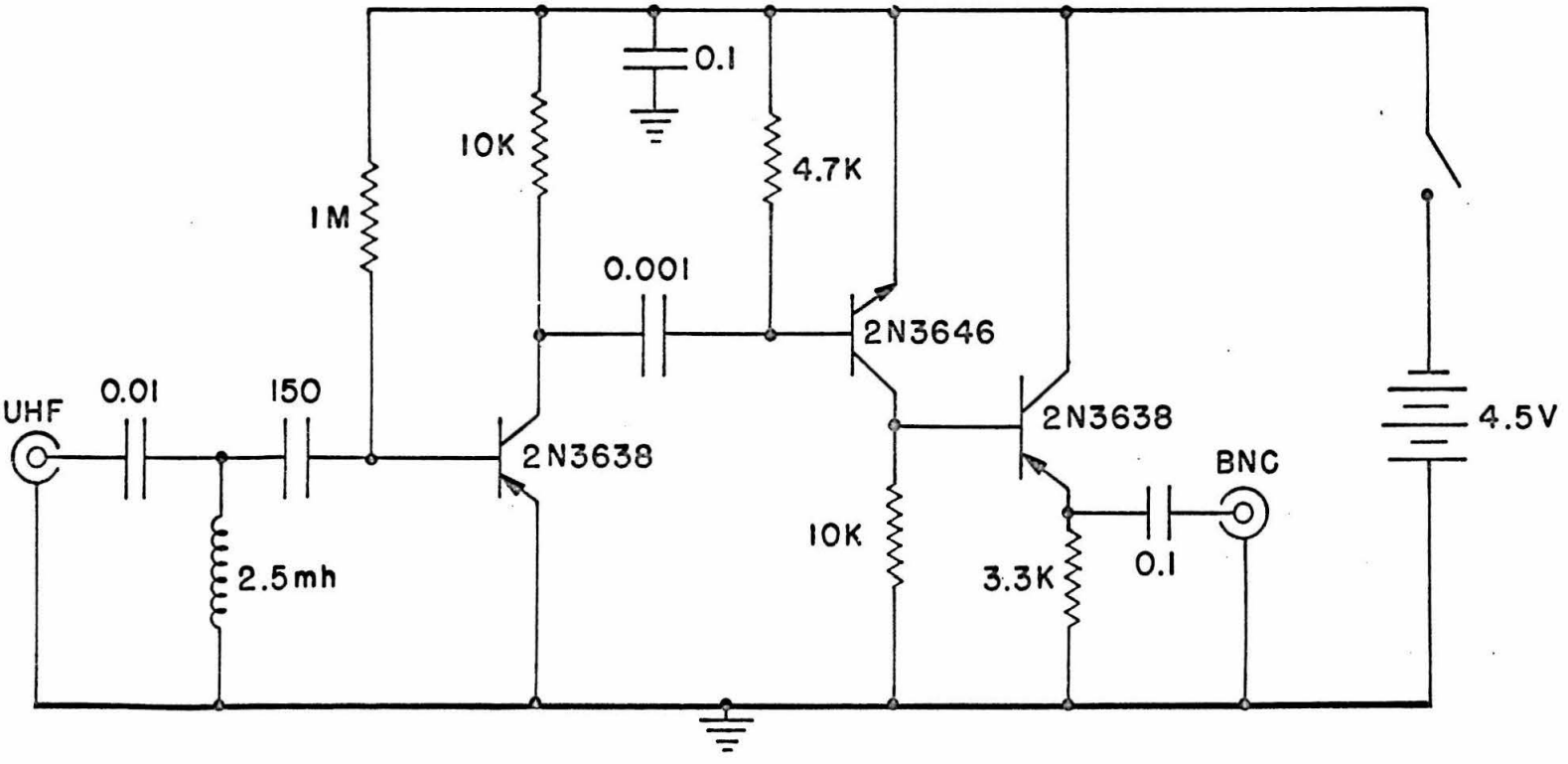

Figure 16

Fig. 17

Modular circuit which includes spark detector gate generator and a count-rate meter. The gate generator takes a signal from the spark detector (fig. 16) and converts it into a pulse capable of blocking the analysis of a pulse in the pulse-shape discriminator (figs. 13-15). Any pulse whose amplitude exceeds 0.5V will drive the count-rate meter, seen below the gate generator. Full-scale ranges of 20, 200, 2k, 20k, and 200k counts/sec are provided. Details of gate generator are found on page 18.

SPARK DETECTOR GATE GENERATOR

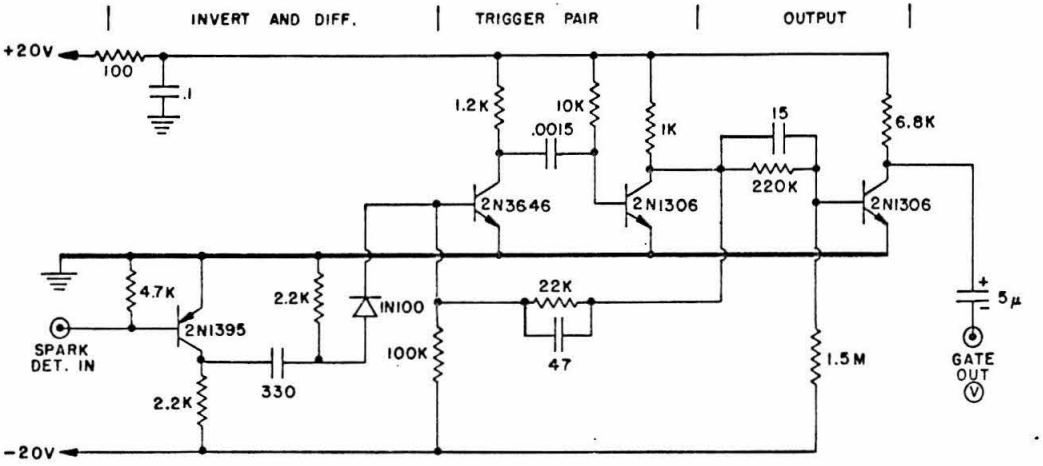

COUNT RATE METER (POSITIVE OR NEGATIVE INPUT)

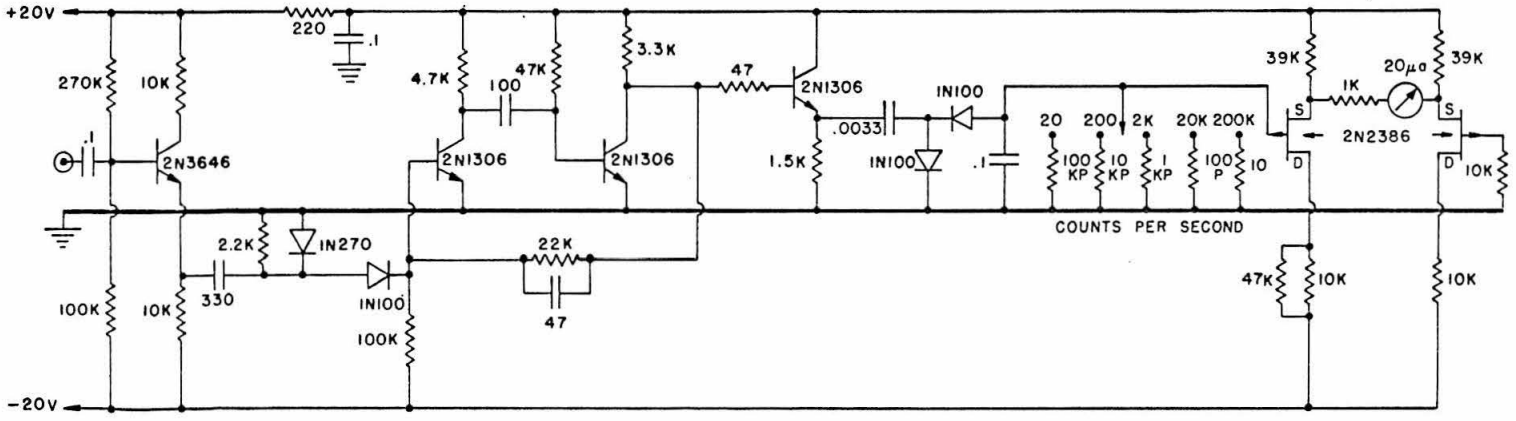

Figure 17

Fig. 18

Illustrating the elimination of the 4.43 MeV gamma ray from the reaction $^{9}Be(\alpha, n_1)^{12}C^*(4.43)$. The lower curve shows the spectrum with the neutron-gamma discriminator in operation, and the upper curve shows the same spectrum when the discriminator is removed. Neutrons from the reaction $^{9}Be(\alpha, n_0)^{12}C$ appear in both spectra in the same number. See page 34.

Figure 18

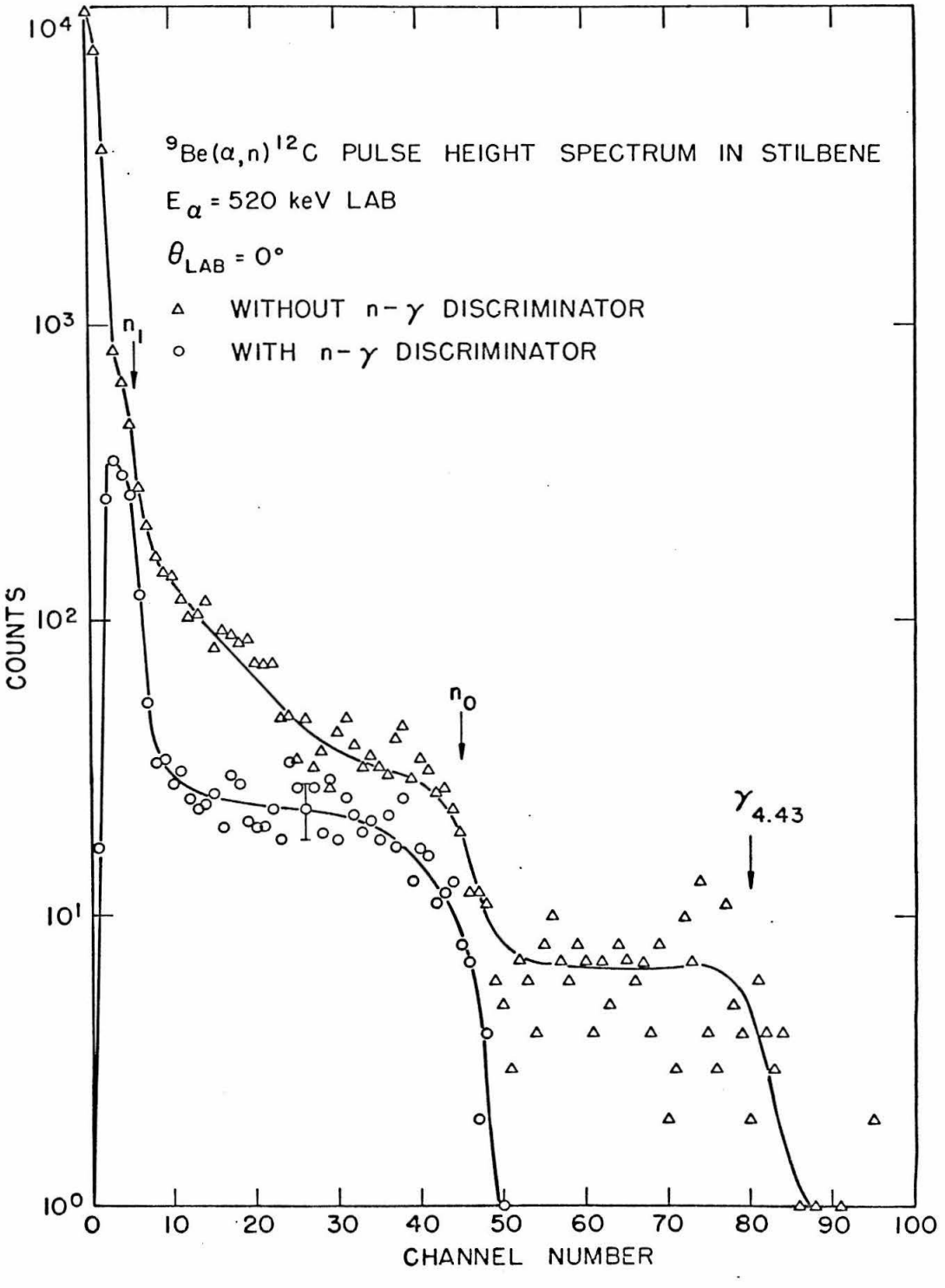
$^{9}Be(\alpha,n)^{12}C$ PULSE HEIGHT SPECTRUM IN STILBENE
E_α = 520 keV LAB
θ_{LAB} = 0°
△ WITHOUT n−γ DISCRIMINATOR
○ WITH n−γ DISCRIMINATOR
n_1
n_0
$\gamma_{4.43}$
COUNTS
CHANNEL NUMBER
10^4
10^3
10^2
10^1
10^0
0
10
20
30
40
50
60
70
80
90
100

Fig. 19

Target-detector geometry for the $^{13}C(\alpha, n)^{16}O$ reaction. See page 12.

Figure 19

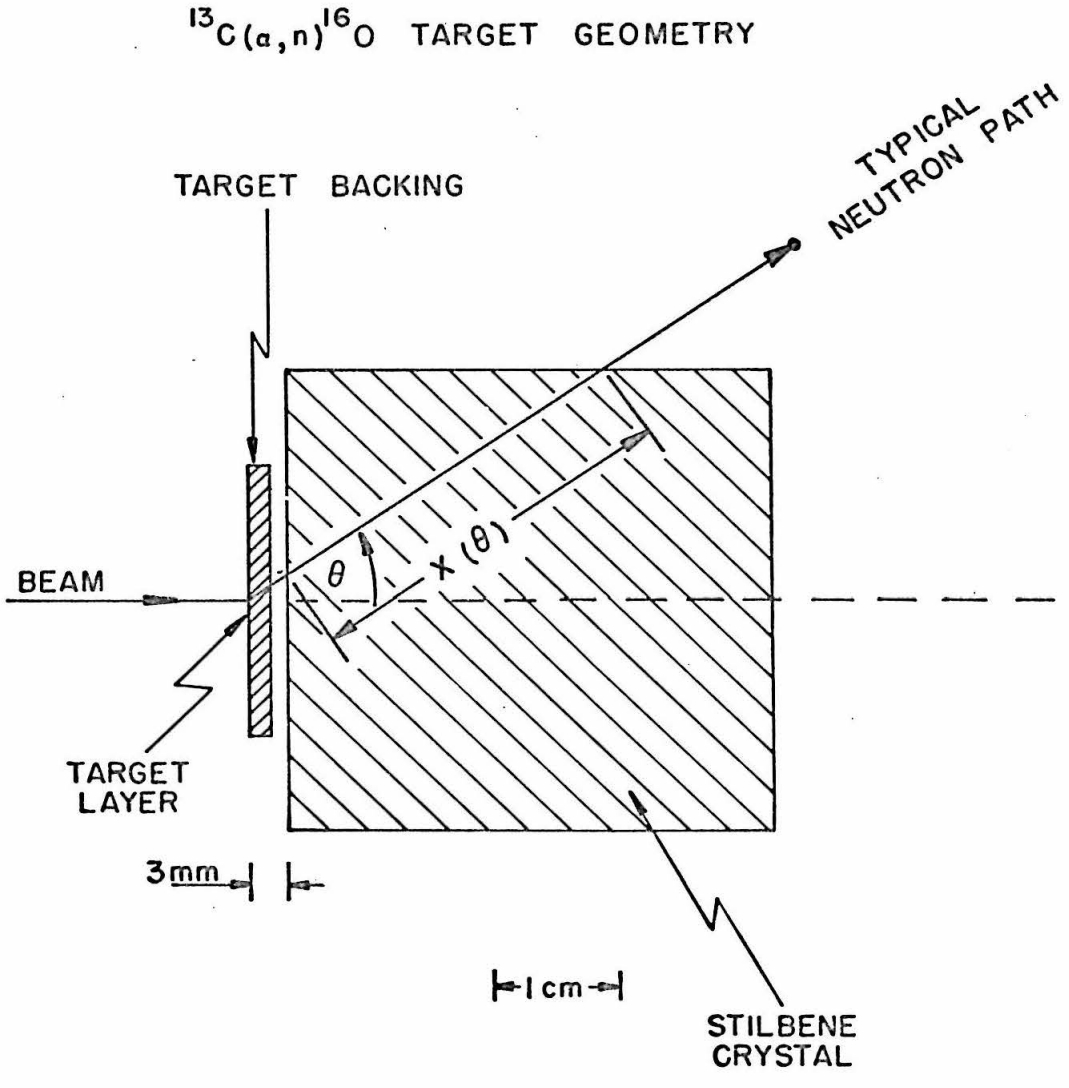
$^{13}C(\alpha,n)^{16}O$ TARGET GEOMETRY
TYPICAL NEUTRON PATH
TARGET BACKING
BEAM
θ
x(θ)
TARGET LAYER
3mm
1 cm
STILBENE CRYSTAL

Fig. 20

Pulse-height spectrum in stilbene of recoil protons from the reaction $^{9}Be(\alpha, n)^{12}C$. Two neutron groups are seen, one leading to the ground state of ^{12}C (n_0), and the other leading to the first excited state (n_1). Also shown on the figure are the cutoff energies E_{c0} and E_{c1} as described on pages 26 and 27.

Figure 20

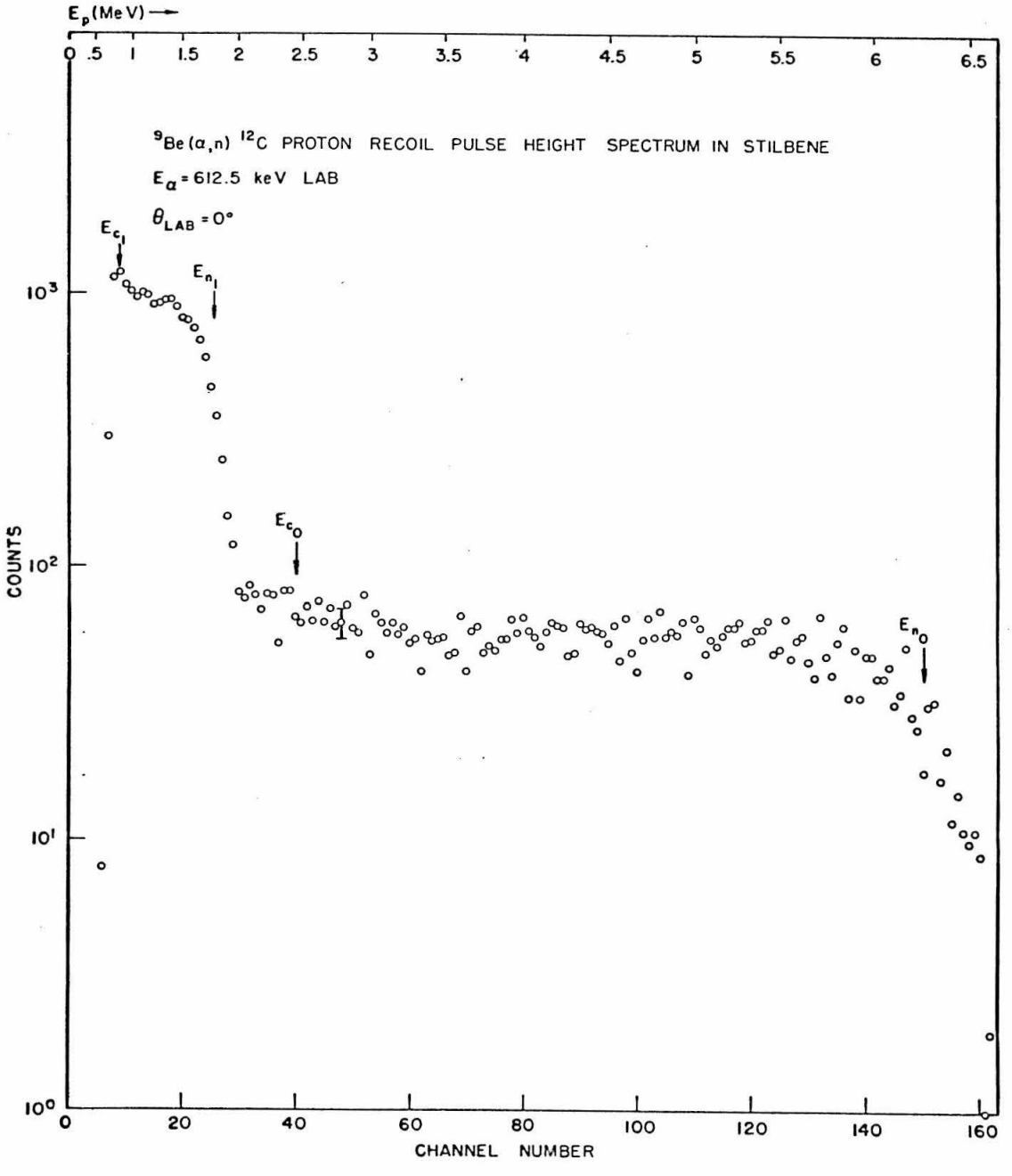
E_p(MeV) →
0 .5 1 1.5 2 2.5 3 3.5 4 4.5 5 5.5 6 6.5
^{9}Be(α,n) ^{12}C PROTON RECOIL PULSE HEIGHT SPECTRUM IN STILBENE
E_α = 612.5 keV LAB
θ_{LAB} = 0°
E_{c_1}
E_{n_1}
E_{c_0}
E_{n_0}
COUNTS
10^3
10^2
10^1
10^0
0 20 40 60 80 100 120 140 160
CHANNEL NUMBER

Fig. 21

Thick-target yield from the reaction $^{13}C(\alpha, n)^{16}O$, in the bombarding energy range 0.475-0.700 MeV. Taken with the geometry shown in fig. 19. The solid curve is computed from the values of S(0) and α obtained from the least-squares fit of the experimental data. See page 32 and Table 1.

Figure 21

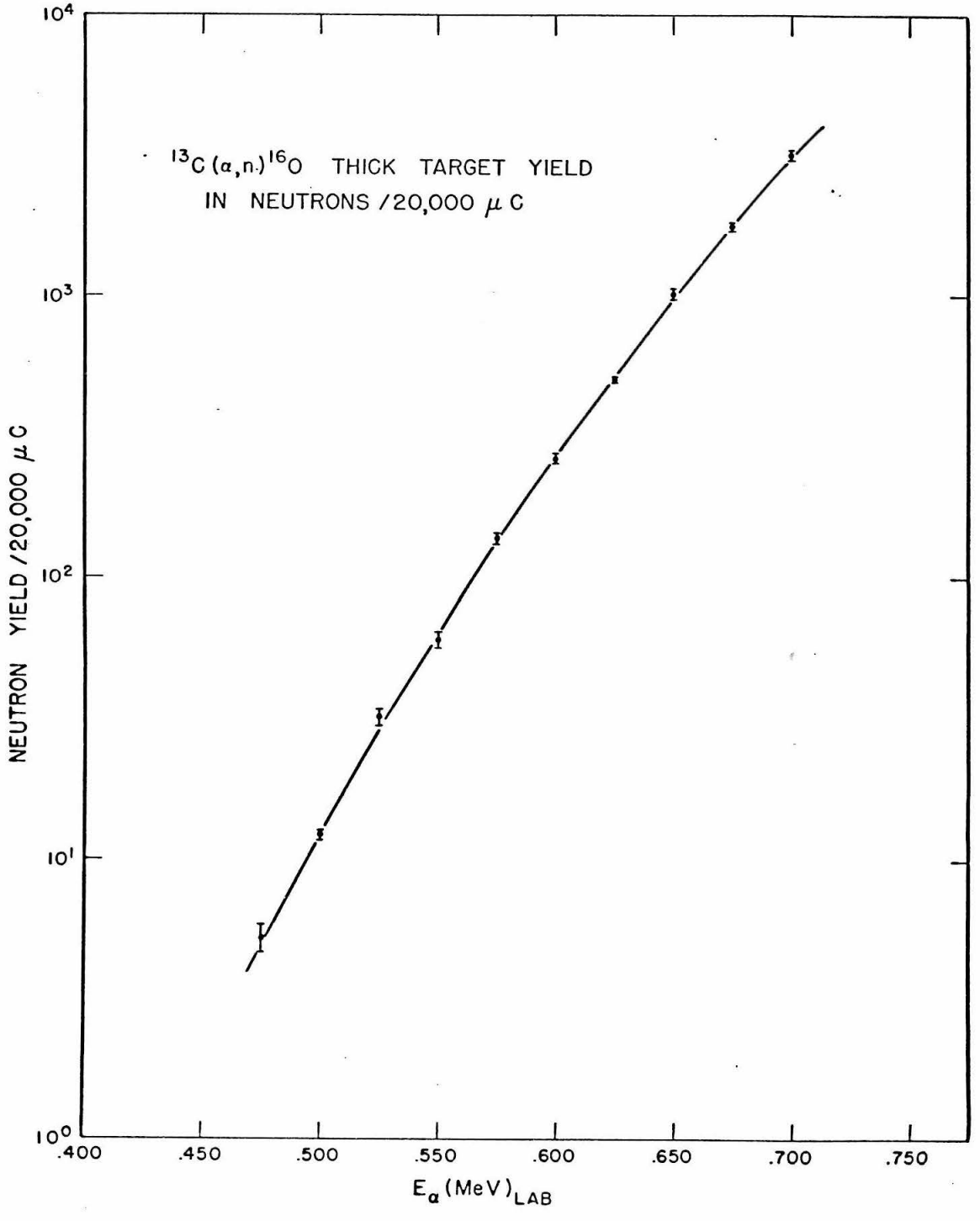
$^{13}C(\alpha,n)^{16}O$ THICK TARGET YIELD
IN NEUTRONS /20,000 μ C
NEUTRON YIELD /20,000 μ C
10^4
10^3
10^2
10^1
10^0
.400
.450
.500
.550
.600
.650
.700
.750
E_α (MeV)$_{LAB}$

Fig. 22

Astrophysical cross-section factor S(E) in the center-of-mass system, calculated from the equation $S(E) = [5.48 + 12.05\ E] \times 10^5$ MeV-barns. The region delineated by arrows indicates the energy range covered in the measurements. See page 26 and Table 1. Errors on the function S(E) are shown by the light curves, as computed from the least-squares fit error matrix.

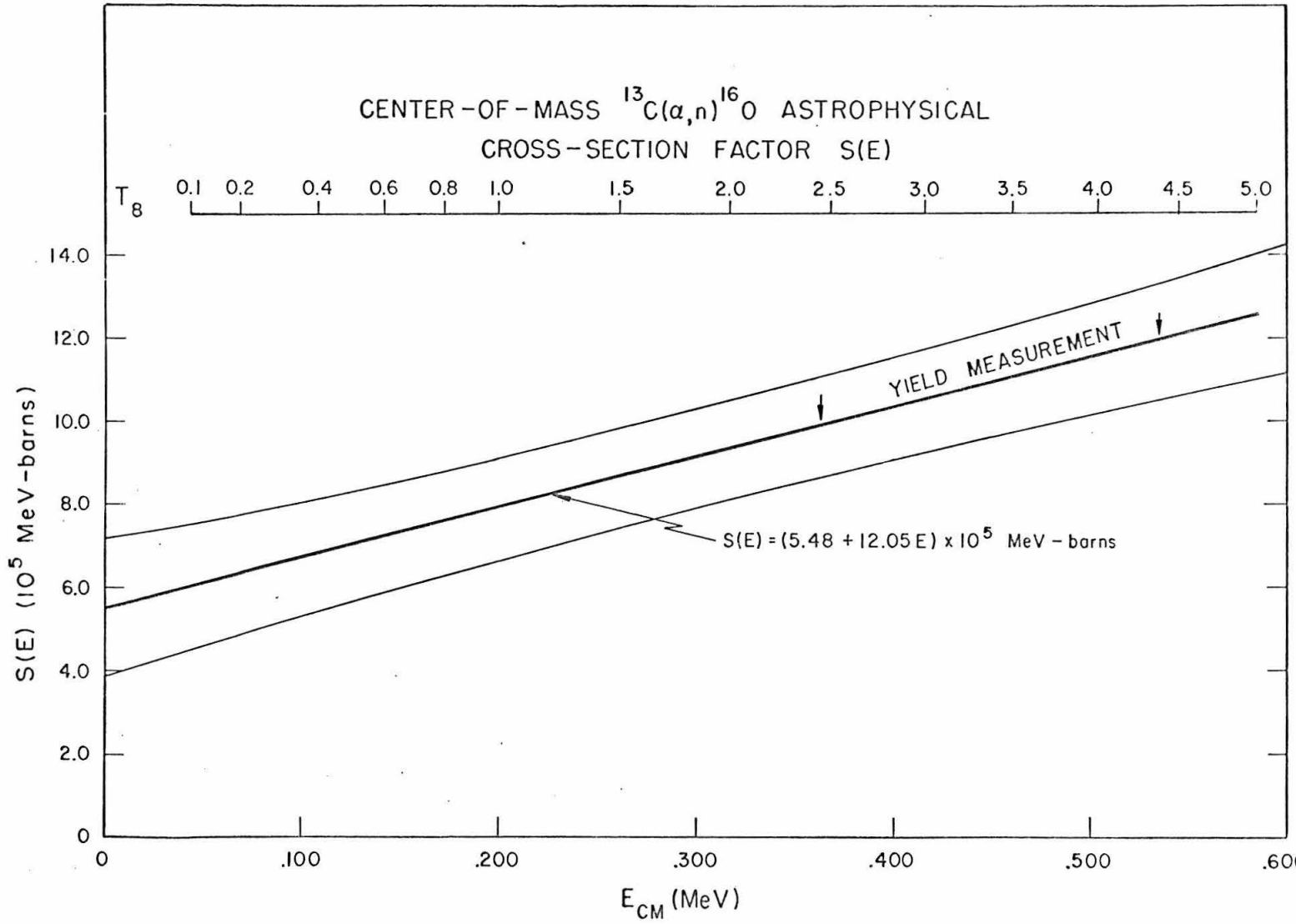
CENTER-OF-MASS $^{13}C(\alpha,n)^{16}O$ ASTROPHYSICAL
CROSS-SECTION FACTOR S(E)
T_8
0.1 0.2 0.4 0.6 0.8 1.0 1.5 2.0 2.5 3.0 3.5 4.0 4.5 5.0
YIELD MEASUREMENT
$S(E) = (5.48 + 12.05\,E) \times 10^5$ MeV - barns
S(E) (10^5 MeV-barns)
14.0
12.0
10.0
8.0
6.0
4.0
2.0
0
0 .100 .200 .300 .400 .500 .600
E_{CM} (MeV)

Figure 22

Fig. 23

Total cross-section in the laboratory system for the reaction $^{13}C(\alpha, n)^{16}O$, calculated from equation 1, page 2. See also page 35 and Table 1.

Figure 23

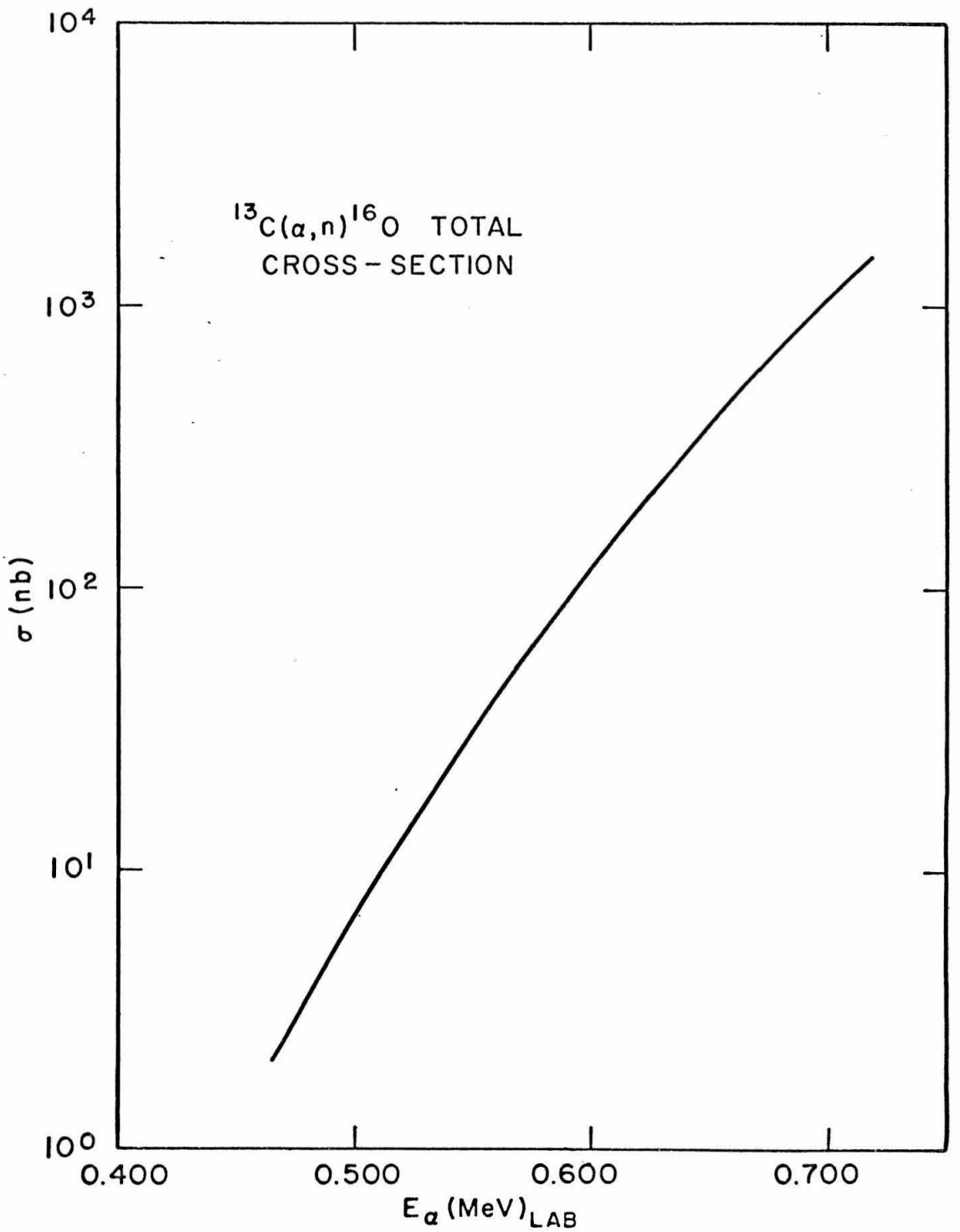
$^{13}C(\alpha,n)^{16}O$ TOTAL
CROSS-SECTION
10^4
10^3
10^2
10^1
10^0
σ (nb)
0.400
0.500
0.600
0.700
E_α (MeV)$_{LAB}$

Fig. 24

Excitation functions at 0^{o} measured for the reactions $^{9}Be(\alpha, n_0)^{12}C$ and $^{9}Be(\alpha, n_1)^{12}C^{*}(4.43)$. The yield has been converted to an absolute differential cross-section by the method outlined in Section (g) (2), part II. See page 33.

Figure 24

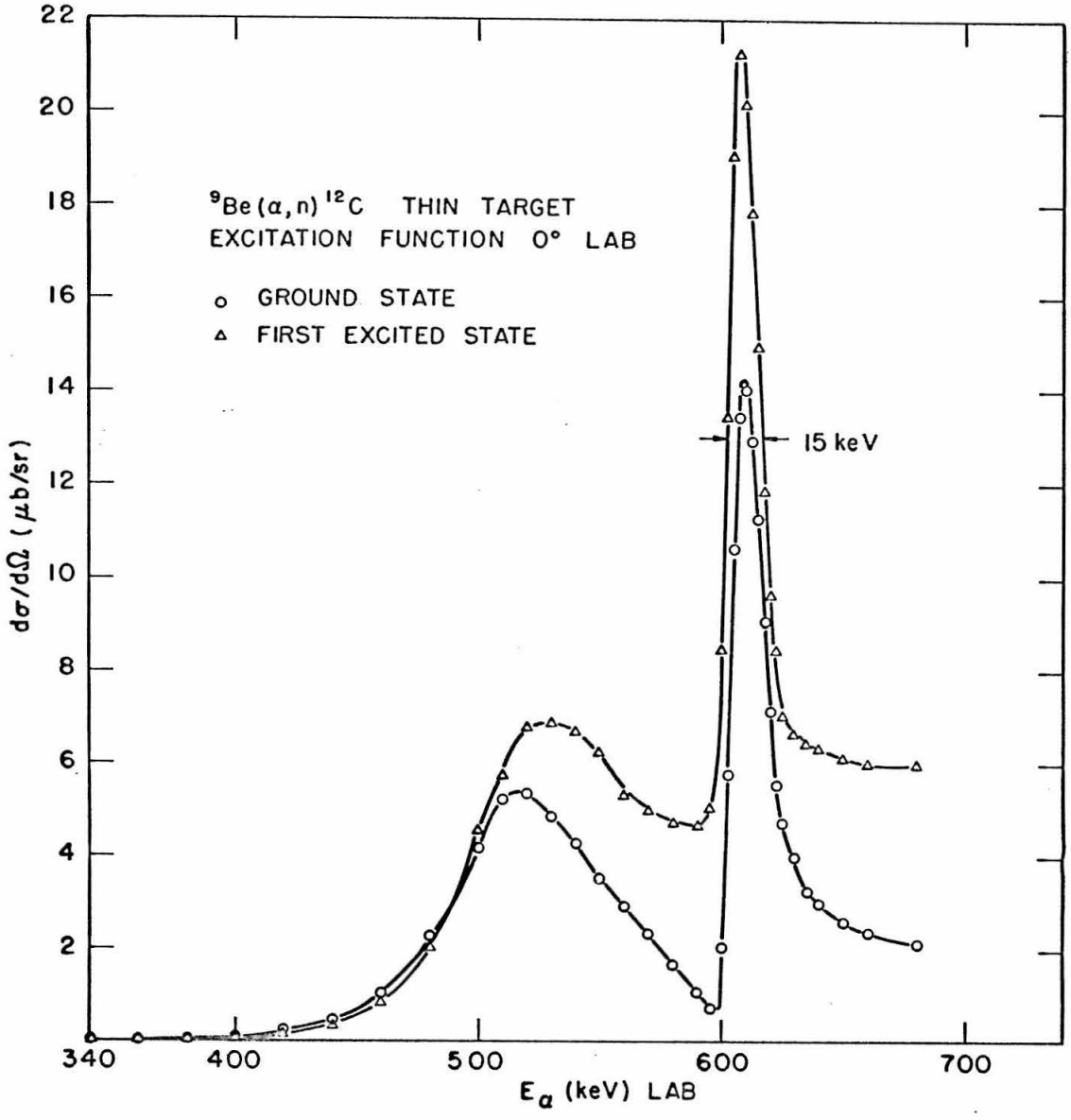
$^{9}Be(\alpha,n)^{12}C$ THIN TARGET
EXCITATION FUNCTION 0° LAB
GROUND STATE
FIRST EXCITED STATE
15 keV
dσ/dΩ (μb/sr)
E_α (keV) LAB
22
20
18
16
14
12
10
8
6
4
2
340
400
500
600
700

Fig. 25

Excitation functions at 90^{o} measured for the reactions $^{9}Be(\alpha, n_0)^{12}C$ and $^{9}Be(\alpha, n_1)^{12}C^{*}(4.43)$. The yield has been converted to an absolute differential cross-section by the method outlined in Section (g) (2), part II. See page 33.

Figure 25

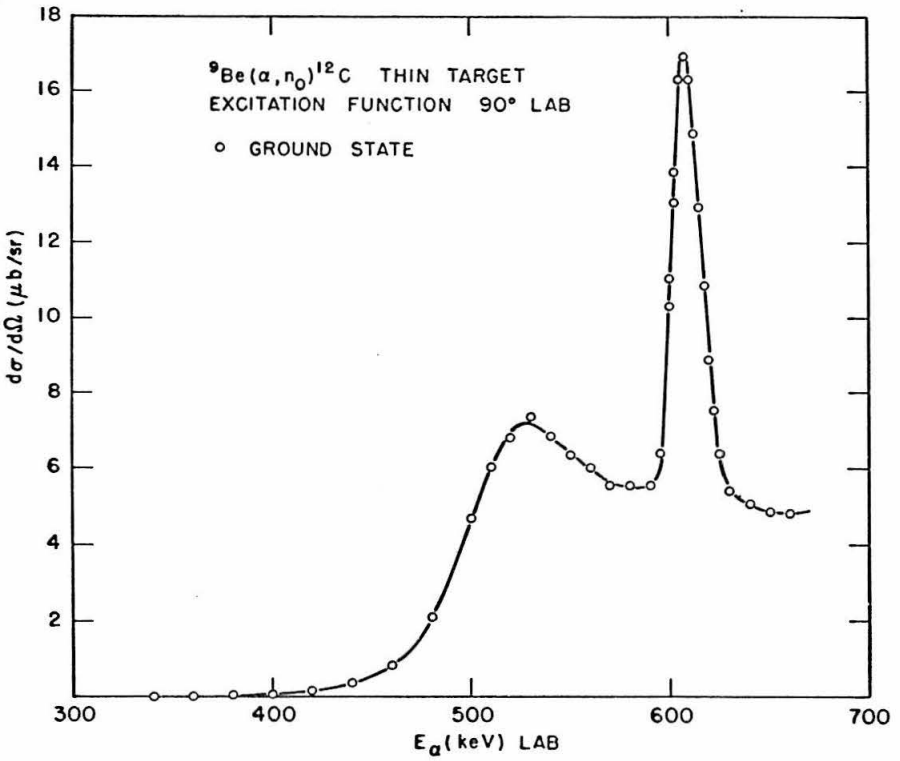
$^{9}Be(\alpha,n_0)^{12}C$ THIN TARGET
EXCITATION FUNCTION 90° LAB
○ GROUND STATE
dσ/dΩ (μb/sr)
E_α (keV) LAB

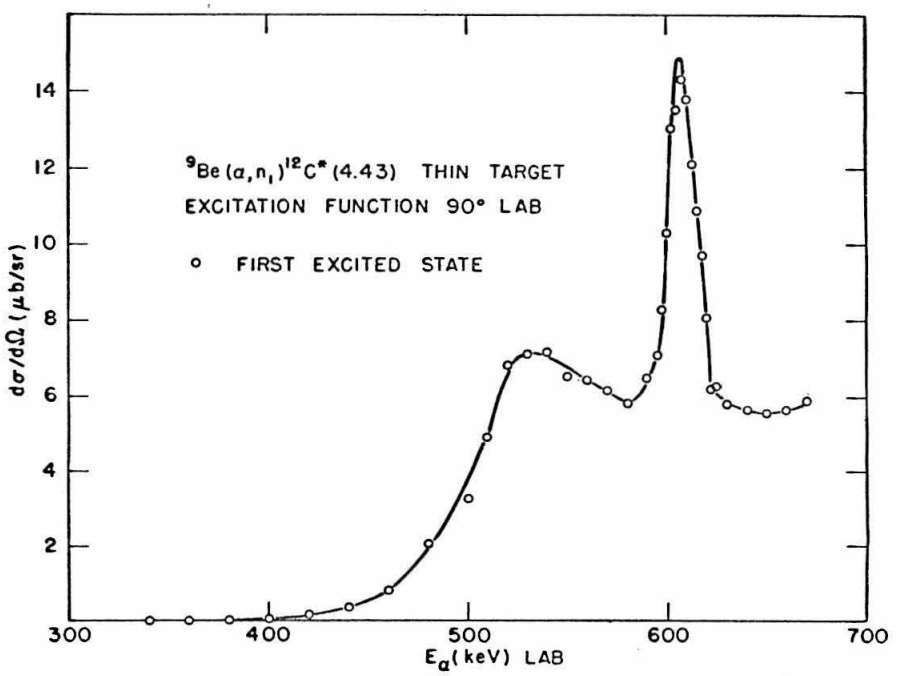
$^{9}Be(\alpha,n_1)^{12}C^*(4.43)$ THIN TARGET
EXCITATION FUNCTION 90° LAB
○ FIRST EXCITED STATE
dσ/dΩ (μb/sr)
E_α (keV) LAB

Fig. 26

Angular distributions for the reaction $^{9}Be(\alpha, n_0)^{12}C$. Shown are the experimental points and the computed fits to Legendre polynomials. See page 33 and Table 2.

Figure 26

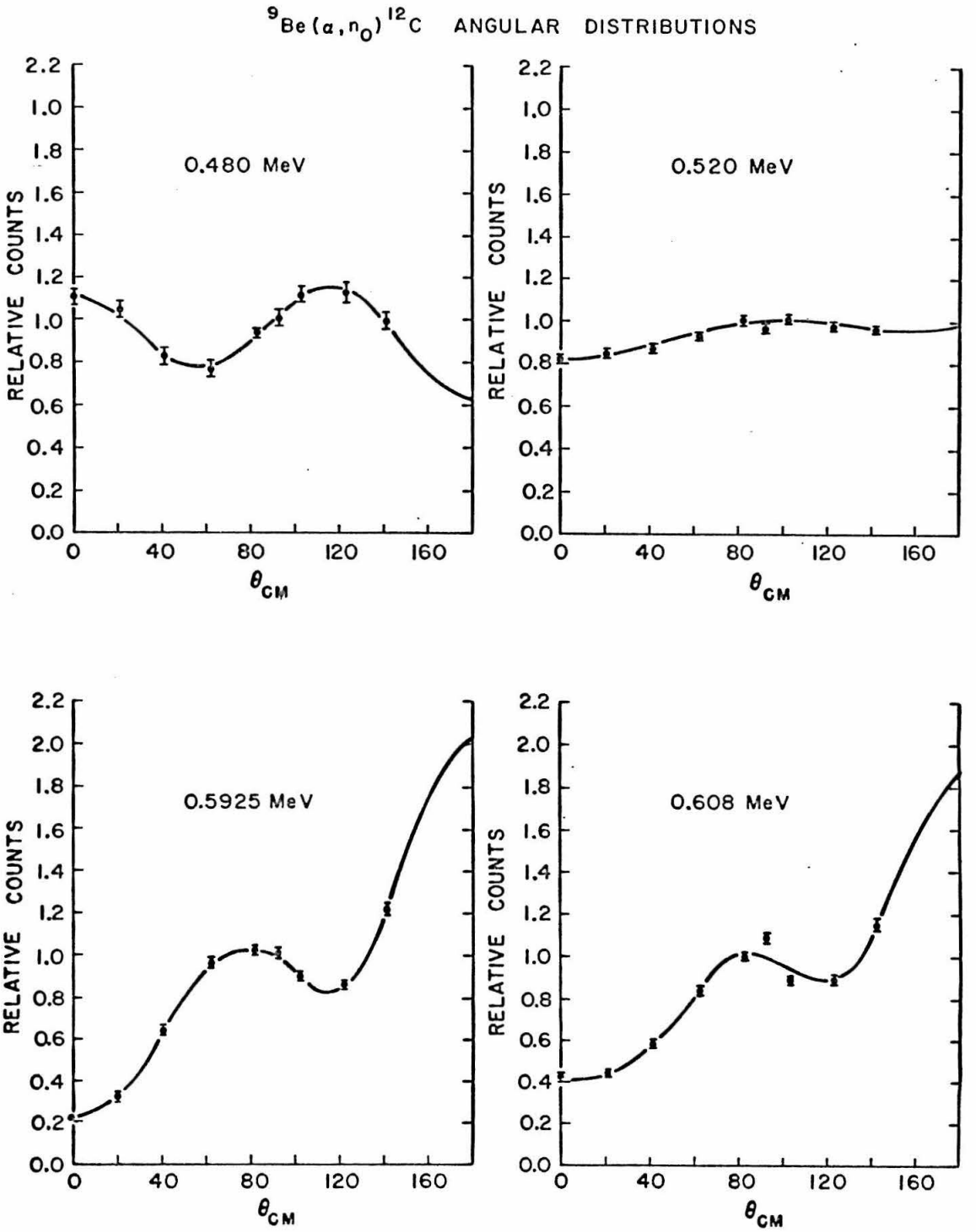
$^{9}Be(\alpha,n_0)^{12}C$ ANGULAR DISTRIBUTIONS
0.480 MeV
0.520 MeV
0.5925 MeV
0.608 MeV
RELATIVE COUNTS
θ_{CM}
0
40
80
120
160
0.0
0.2
0.4
0.6
0.8
1.0
1.2
1.4
1.6
1.8
2.0
2.2

Fig. 27

Angular distributions for the reaction $^{9}Be(\alpha, n_1)^{12}C^*$ (4.43). Shown are the experimental points and the computed fits to Legendre polynomials. See page 33 and Table 2.

Figure 27

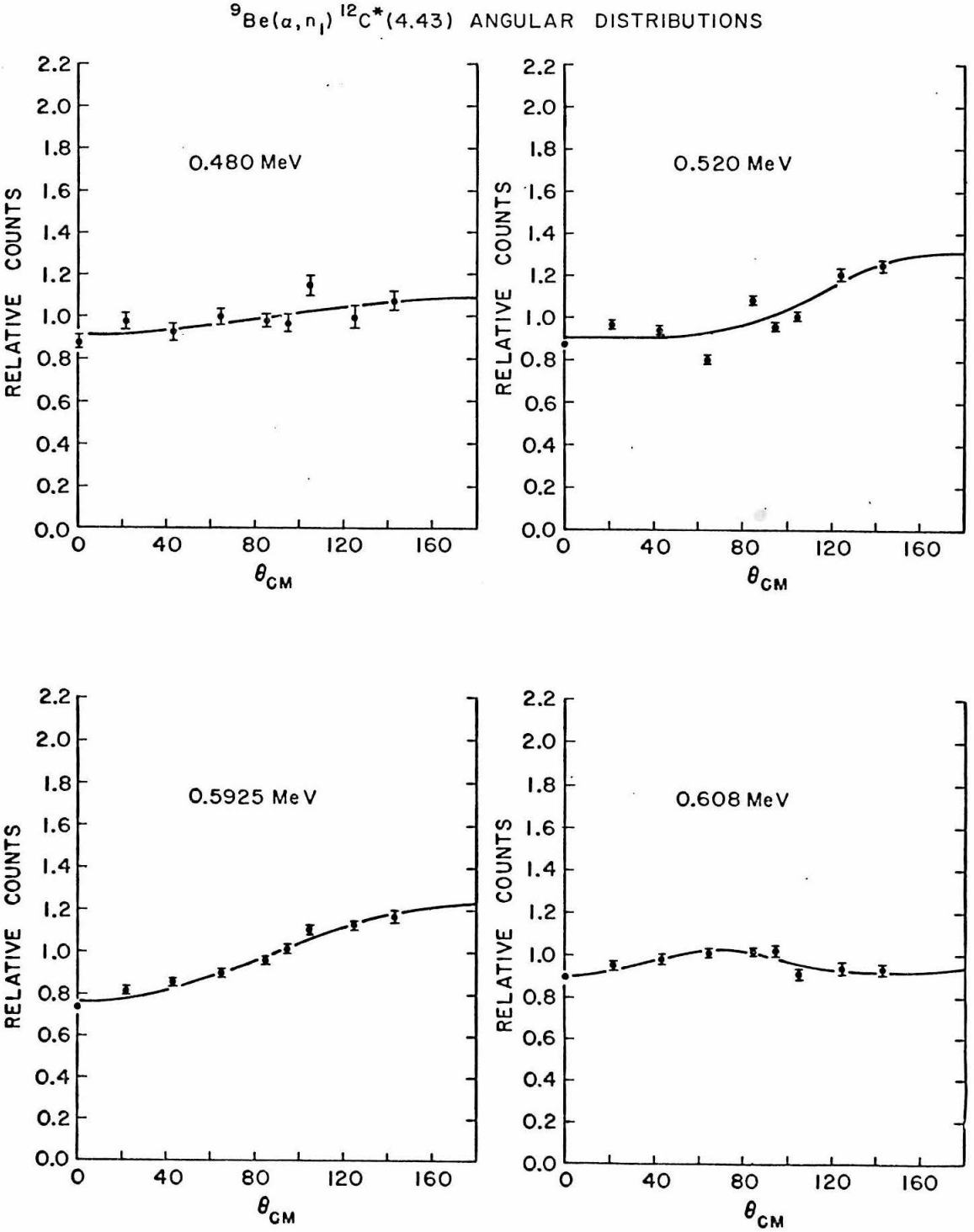
$^{9}Be(\alpha,n_1)\,^{12}C^{*}(4.43)$ ANGULAR DISTRIBUTIONS
0.480 MeV
0.520 MeV
0.5925 MeV
0.608 MeV
RELATIVE COUNTS
θ_{CM}
0.0
0.2
0.4
0.6
0.8
1.0
1.2
1.4
1.6
1.8
2.0
2.2
0
40
80
120
160

Fig. 28

Lifetime of the ^{13}C nucleus to interaction with ^{4}He. The quantity plotted is $\log_{10}[\rho X_{^4He} \tau_{^4He}(^{13}C)]$, with τ given in years, ρ in gm-cm^{-3}, and $X_{^4He}$ is the mass fraction of ^{4}He. See page 45 and Table 3.

Figure 28

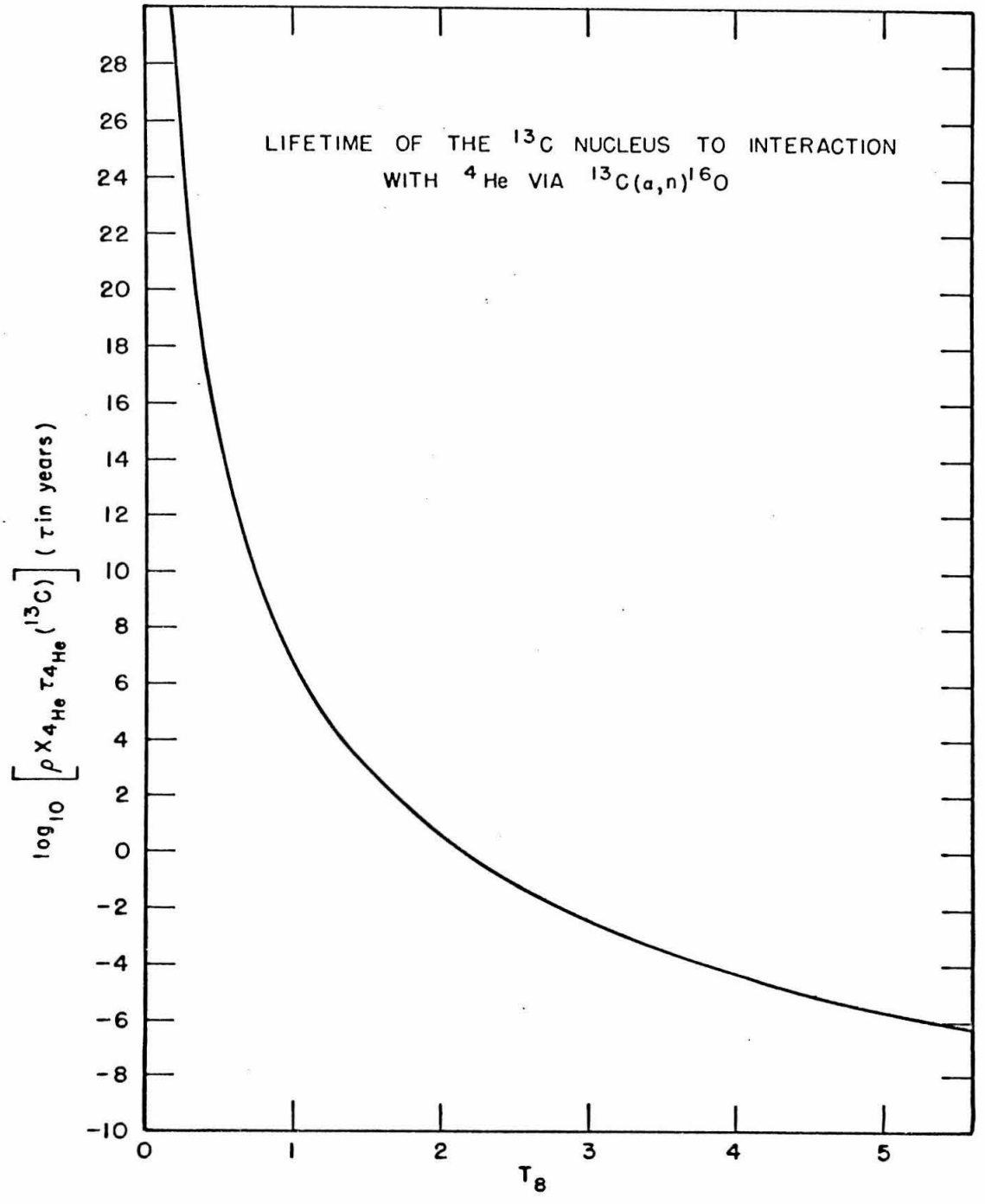
LIFETIME OF THE ^{13}C NUCLEUS TO INTERACTION WITH ^{4}He VIA $^{13}C(\alpha,n)^{16}O$
$\log_{10}\left[\rho X_{^4He}\tau_{^4He}(^{13}C)\right]$ (τ in years)
28
26
24
22
20
18
16
14
12
10
8
6
4
2
0
-2
-4
-6
-8
-10
0
1
2
3
4
5
T_8